Deep–Sea Research I 187 (2022) 103834

Contents lists available at ScienceDirect

Deep-Sea Research Part I

journal homepage: www.elsevier.com/locate/dsri

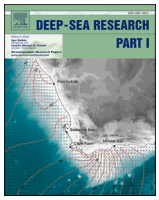

Seasonal cycles of phytoplankton and net primary production from Biogeochemical Argo float data in the south-west Pacific Ocean

Stephen M. Chiswell [a,*], Andrés Gutiérrez-Rodríguez [a], Mark Gall [a], Karl Safi [b], Robert Strzepek [c], Moira R. Décima [a,d], Scott D. Nodder [a]

[a] National Institute of Water and Atmospheric Research, Private Bag 14-901, Wellington, New Zealand
[b] National Institute of Water and Atmospheric Research, PO Box 11115, Hillcrest, Hamilton, New Zealand
[c] Australian Antarctic Program Partnership, Institute for Marine and Antarctic Studies, University of Tasmania, Hobart, Tasmania, Australia
[d] Scripps Institution of Oceanography Department, La Jolla, CA, 92093, USA

ARTICLE INFO

Keywords:
Primary production
BGC-Argo floats
Physical control
Pacific Ocean
New Zealand
Subtropical water
Subantarctic water
Subantarctic mode water

ABSTRACT

We present annual cycles of chlorophyll *a*, phytoplankton carbon, nitrate and oxygen for Subtropical (STW), Subantarctic (SAW), and Subantarctic Mode (SAMW) waters near Aotearoa New Zealand from data collected by two Biogeochemical (BGC) Argo floats. We develop two simple models of depth-integrated net primary production (NPP), tuned against ^{14}C-uptake measurements, to compare with Vertically-Generalised Production Model (VGPM) satellite-based estimates of NPP. One model is the simplest possible, and assumes production is proportional to light multiplied by chlorophyll *a* concentration. The second model modifies the light response profile to account for photoacclimation. In STW at 30–35°S, enhanced production is initiated in austral autumn when the mixed layer deepens to entrain nutrients into the photic zone. For about half the year, there is substantial production within a deep chlorophyll maximum that sits below the mixed layer. Consequently, depth-integrated NPP is only loosely related to surface biomass as imaged from satellite remote-sensing, and BGC Argo-based model estimates of depth-integrated NPP are about double VGPM estimates. In SAW at 45–55°S, production is initiated when vertical mixing decreases in austral spring. Production is largely within the mixed layer, and depth-integrated phytoplankton biomass and depth-integrated NPP follow surface phytoplankton biomass. Model estimates of depth-integrated NPP based on BGC Argo float profiles are comparable with VGPM estimates for the southern water masses.

1. Introduction

Net primary production (NPP) in the oceans, and the physical and biological mechanisms driving this production have long been of interest because changes in NPP strongly affect higher trophic levels, with consequent flow-on effects on ecosystem structure and functioning (e.g., Chassot et al., 2010; Stock et al., 2017). Climate change has been projected to affect NPP both positively and negatively, depending on the regional physical and biological processes driving the production (e.g., Bopp et al., 2013; Krumhardt et al., 2017; Law et al., 2017). There is consequently a need for better regional understanding of the seasonal cycles of primary production, and how NPP responds to environmental forcing that may be influenced by climate change, such as air-sea heat fluxes, ocean warming, stratification, mixed-layer depth, and nutrient fluxes.

Various ocean colour satellite products have been derived to estimate NPP. In particular, the Vertically-Generalised Production Model (VGPM, Behrenfeld and Falkowski, 1997a; Behrenfeld and Falkowski, 1997b) has been used in climate prediction studies (e.g., Taboada et al., 2019), regional studies (e.g., Kahru et al., 2009), process studies (e.g., Milutinović et al., 2009), and global analyses (e.g., Tseng et al., 2019). However, it has long been recognised that satellite observing sensors are unable to detect subsurface structure in phytoplankton biomass, potentially resulting in errors in the depth-integrated biomass and depth-integrated NPP. In addition, ocean-colour based models are challenged by high-nutrient low-chlorophyll *a* (Chl) conditions, and/or extreme temperatures (Carr et al., 2006). Partly in order to address these issues, the Biogeochemical-Argo program (BGC-Argo, Claustre et al., 2020) was developed to maintain a global network of profiling floats making key measurements of Chl fluorescence, particulate organic

* Corresponding author.
E-mail address: s.chiswell@niwa.cri.nz (S.M. Chiswell).

https://doi.org/10.1016/j.dsr.2022.103834
Received 2 July 2021; Received in revised form 30 May 2022; Accepted 2 July 2022
Available online 7 July 2022

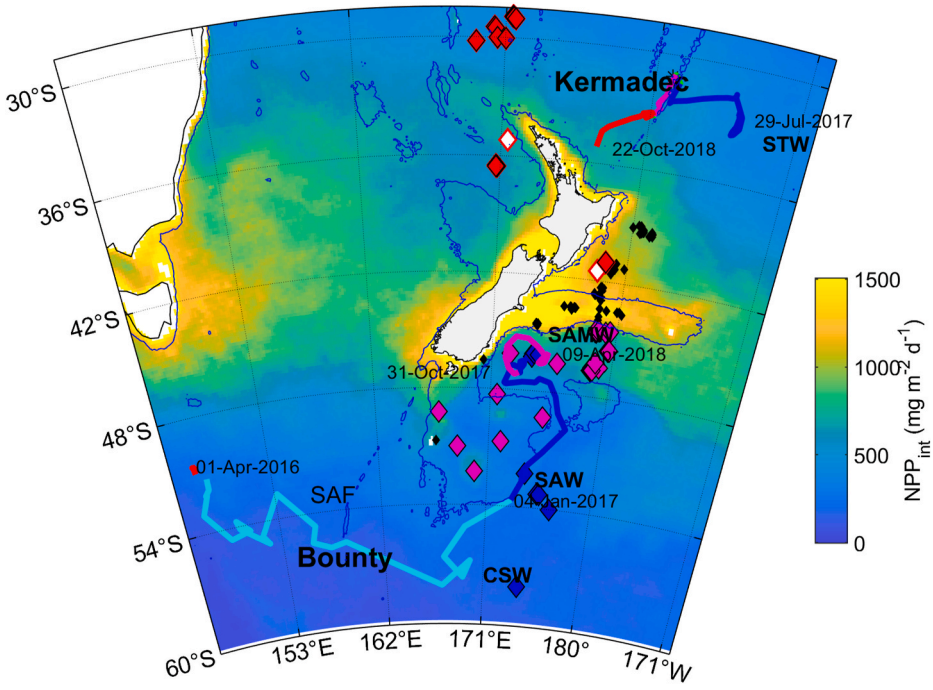

Fig. 1. Trajectories of the Kermadec and Bounty Biogeochemical Argo floats superimposed over the 2016/2017 mean depth-integtated net primary production (NPP_{int}) as estimated by the Vertically Generalised Production Model (VGPM). Trajectories are colour-coded according to the T-S properties seen in each float profile (see Fig. 2). Surface waters are Subtropical Water (STW), Subantarctic Mode Water (SAMW), Subantarctic Water (SAW), and Circumpolar Surface Water (CSW). SAF indicates the Subantarctic Front separating CSW from SAW. Also shown are locations of all ^{14}C-uptake measurements of NPP (black diamonds), and those used to tune the models (red in STW, blue in SAW, and magenta in SAMW).

carbon (POC), and nitrate (NO_3), as well as other standard parameters - depth, temperature (T), salinity (S), and dissolved oxygen (O_2).

In this article, we investigate how the temporal and vertical variability in primary production can be estimated from BGC-Argo floats. To do this, we develop two models of NPP that are tuned against *in situ* ^{14}Carbon (^{14}C)-uptake measurements made in the south-west Pacific Ocean near Aotearoa New Zealand over the last 25 years.

While many BGC-Argo floats have passed through the New Zealand region, only two floats have measured all the variables of interest - Chl, POC, NO_3, and O_2. The first float sampled Subtropical Water (STW) to the north-east of New Zealand, and the second float sampled Circumpolar Surface Water, Subantarctic Water (SAW), and Subantarctic Mode Water (SAMW), to the south of New Zealand (Fig. 1). Water masses are considered to be different biomes reflecting the different roles that nutrients, light, and mixing play in controlling production (e.g., Boyd et al., 1999; Longhurst, 2007), and while there have been several regional process and satellite-based studies of ecosystem functioning in these water masses (e.g., Bradford-Grieve et al., 1999; Chiswell et al., 2015; Ellwood et al., 2015; Murphy et al., 2001; Nodder et al., 2005; Nodder et al., 2016), these BGC-Argo floats provide the first data that allow estimates to be made of the seasonal cycles of the depth-structure of phytoplankton biomass, production, and their environmental forcing.

The aims of this article are two-fold. The first aim is to provide the seasonal cycles of the vertical structure of nutrients, phytoplankton biomass, and primary production for these water masses, and to relate these seasonal cycles to physical forcing mechanisms. The second aim is to develop two regionally focussed models of NPP tuned against *in situ* ^{14}C-uptake measurements. The first model is the simplest possible model where primary production at depth is proportional to *in situ* light multiplied by chlorophyll concentration. The second model replaces light with an equation based on Behrenfeld et al. (2005) that flattens the exponential decay of light near the surface to account for light photoacclimation. These models are not meant to be mechanistic models of NPP; instead, they are designed to provide a phenomenological view of the important processes leading to biological primary production, and to aid in the investigation of how well VGPM and other satellite-based algorithms likely perform in such regional settings.

1.1. Estimating NPP from BCG-argo data

It is commonly assumed that net primary production is functionally proportional to phytoplankton concentration (e.g., Sathyendranath et al., 2009), so that the rate of change of phytoplankton biomass at depth, z, can be written as

$$\partial C_P(z)/\partial t = \mu(z)C_P(z) - l(z)C_P(z), \quad (1)$$

where $NPP = \mu(z)C_P(z)$, C_P is the phytoplankton biomass (mg C m^{-3}), μ and l are the specific (i.e. per unit C_P) production and loss (grazing, mixing, advection) rates, both having units d^{-1}. All values are daily-mean values.

We compute estimates of depth-integrated NPP (which has also been also termed areal NPP) for the two models by integrating the depth-dependent NPP,

$$NPP_{inti} = \int NPP_i dz = \int \mu_i C_P dz, \quad (2)$$

where NPP_{inti} is the depth-integrated NPP having units mg C m^{-2} d^{-1}, and subscript i indicates the model.

The specific production rate, μ, has been modelled in a variety of ways of differing complexity reflecting plankton species composition, photoacclimation and nutrient levels, and temperature (e.g., Aumont et al., 2015; Behrenfeld et al., 2005; Li et al., 2010; Litchman and Klausmeier, 2008; Yang et al., 2020), but here, the aim is to develop models that avoid as much complexity as possible.

Model 1 is the simplest possible model, and assumes the specific production rate at depth is proportional to the local downwelling light intensity, I (units mol m^{-2} d^{-1}), multiplied by the chlorophyll to carbon ratio, [Chl: C_P],

$$\mu_1 = \nu_1 I[Chl : C_P], \quad (3)$$

where ν_1 is a scaling factor (mol^{-1} m^2), and the light intensity decays approximately exponentially with depth according to the Beer-Lambert law (e.g. Weiskerger et al., 2018).

Model 2 replaces I in Eq. (3) with a 'light function' (no units) designed to incorporate photoacclimation in the upper water column by

flattening the exponential decay of light near the surface,

$$\mu_2 = \nu_2(1 - exp(-nI))/(1 + exp(-nI)) \left[Chl : C_p\right] , \quad (4)$$

where n is a tuneable coefficient that flattens the light function more as n increases. Eq. (4) is a simplified version of the Behrenfeld et al. (2005) equation with a scaling factor ν_2 (d^{-1}).

The coefficients n and ν_i are assumed to be constant in time and depth and can be chosen to minimise the difference between model estimates and ^{14}C-uptake measurements as discussed in the Supporting Information.

The depth-integrated loss rates, L (mg C m^{-2} d^{-1}), can be derived as

$$L_i = NPP_{inti} - \partial/\partial t \int C_P dz . \quad (5)$$

2. Data and methods

2.1. BGC-argo profiles

BGC-Argo floats (Claustre et al., 2020) profile between 2000 m and the sea-surface about every 10 d. Between profiles, the floats drift at a depth of 1000 m, so their trajectories are largely determined by ocean lateral velocity at 1000 m, but are also affected by the velocities seen during profiling.

Core variables measured by BGC-Argo include Chl, POC, NO_3, and O_2. Details of how these quantities are measured are provided by Claustre et al. (2020) and Johnson et al. (2017a). In summary, Chl is estimated from fluorescence, POC is estimated from optical backscatter at 700 nm (b_{bp700}), NO_3 is estimated from ultraviolet absorbance spectra, and O_2 is estimated from Clark-type electrodes or fluorescence optodes.

Here, high resolution quality-controlled data were downloaded from the Southern Ocean Carbon and Climate Observations and Modeling (SOCCOM) programme. Data from two floats WMO 5905108 and 5904677 were chosen because these floats had the most complete data sets in the New Zealand region. However, the salinity sensor failed for both floats, and because salinity was used to determine water mass, data were only used up to the point of sensor failure.

The core phytoplankton biomass variable reported by SOCCOM is POC derived as a linear function of b_{bp700}. Backscatter can also be used to estimate the phytoplankton carbon biomass, C_P, and based on (Graff et al., 2015), we estimate C_P as

$$C_P = 12128 b_{bp470} + 0.59 , \quad (6)$$

where, following Boss et al. (2013) and Boss and Haëntjens (2016), the backscatter at 470 nm is estimated from the backscatter at 700 nm as

$$b_{bp470} = b_{bp700}\left(\frac{470}{700}\right)^{-0.78} . \quad (7)$$

Thus, C_P and POC are both linear functions of b_{bp700}, but have different slopes and different intercepts. Averaged over both floats, C_P was about 46% of POC.

BGC-Argo float surface times slowly change through the deployment. Consequently, many surface times were during daylight hours, resulting in profiles having chlorophyll missing in the upper 100 m due to non-photochemical quenching (e.g., Carberry et al., 2019). Rather than correcting for quenching (e.g., Thomalla et al., 2018; Xing et al., 2012), we report Chl and [Chl:C_P] using the gappy records. For the models, and to compute light extinction coefficient (see later), we filled the gaps in Chl by multiplying C_P by a mean estimate of [Chl:C_P] derived from all available data for each float. Any remaining gaps were filled by linear interpolation.

Near-surface values of all variables were taken to be the values at 10 m depth (Chl_{10}, C_{P10}, etc). Virtually all production is in the upper 200 m (see later), so depth-integrated values were computed by integrating from the surface to 300 m (e.g., $C_{P0/300} = \int_0^{300} C_P dz$).

Two estimates of mixed-layer depth, MLD_{03} and MLD_{125}, were computed as the shallowest depth where the density exceeds the surface density by 0.030 kg m^{-3} and 0.125 kg m^{-3}, respectively (e.g., Kara et al., 2000). MLD_{125} has been considered to define the seasonal thermocline (Suga et al., 2004), whereas MLD_{03} may be a better indicator of mixed layers relevant to phytoplankton blooms (Chiswell, 2011).

Specific accumulation rates, $r_{10} = \partial \ln C_{P10}/\partial t$, and $r_{0/300} = \partial \ln C_{P0/300}/\partial t$ (units d^{-1}), for near-surface (10 m) and depth-integrated (0–300 m) phytoplankton carbon were smoothed with a 60-day window. Most other quantities were smoothed with a 20-day window. These window lengths were chosen to smooth out noise due to measurement errors and patchiness in the data. (Time-derivatives are by their very nature are more noisy, and require longer window lengths than their respective time series).

2.2. Sea-surface chlorophyll, PAR, and VGPM

Moderate Resolution Imaging Spectroradiometer (MODIS) Aqua 9-km, 8-d, composite sea surface chlorophyll (SSC) and daily-mean photosynthetically active radiation (PAR) were downloaded from NASA's Ocean Color web site. The 9-km, 8-d VGPM data were downloaded from the Ocean Productivity website at Oregon State University.

Time series of SSC, VGPM, and PAR following the float locations were computed by choosing the closest estimates in space and time to the locations (i.e., at the point closest to where the float surfaced, at the time closest to the surface time). These closest estimates could be up to 4 d different in time. Often the SSC satellite data were missing due to clouds. VGPM estimates of depth-integrated NPP were also obtained for each ^{14}C-uptake measurement by choosing the closest estimates in space and time to the locations to the uptake measurement location.

Light profiles, $I(z)$, for each float profile were computed by numerically integrating the attenuation equation,

$$dI = k_d dz , \quad (8)$$

using MODIS-derived values of PAR (mol m^{-2} d^{-1}) for the surface value (i.e., $I(0) = PAR$), where k_d is the diffuse light attenuation coefficient. PAR is weighted over several wavelengths (400–700 nm). Hence, as an approximation to integrating over all wavelengths, k_d was computed as the mean of the 490 nm and 690 nm values, being wavelengths of absorption peaks in chlorophyll, $k_d = (k_{d490} + k_{d690})/2$. Attenuation coefficients were computed as a function of chlorophyll (Morel and Maritorena, 2001),

$$k_{d490} = 0.0166 + 0.07274 Chl^{0.6896} \text{ and}$$
$$k_{d690} = 0.05164 + 0.0390 Chl^{0.640} . \quad (9)$$

2.3. Surface air-sea heat fluxes

The net air-sea heat flux, Q_f (W m^{-2}) was computed as the sum of long-wave, short-wave, sensible and net-heat fluxes. Daily-mean values of these fluxes were obtained from the National Centers for Environmental Prediction (NCEP) reanalysis products (Kalnay et al., 1996).

Time series of Q_f along the float tracks were computed by choosing the daily value closest in space and time to the floats' surface locations. Positive Q_f represents heat entering the atmosphere, negative values represent ocean warming.

2.4. ^{14}C-uptake measurements of NPP

^{14}C-uptake measurements of NPP have been made since 1995, mostly east of New Zealand (Fig. 1 and Table S1). The experimental set-up, and sample processing differed between cruises. However, in general, 24-h experiments were run in light and dark bottles (320 mL acid-

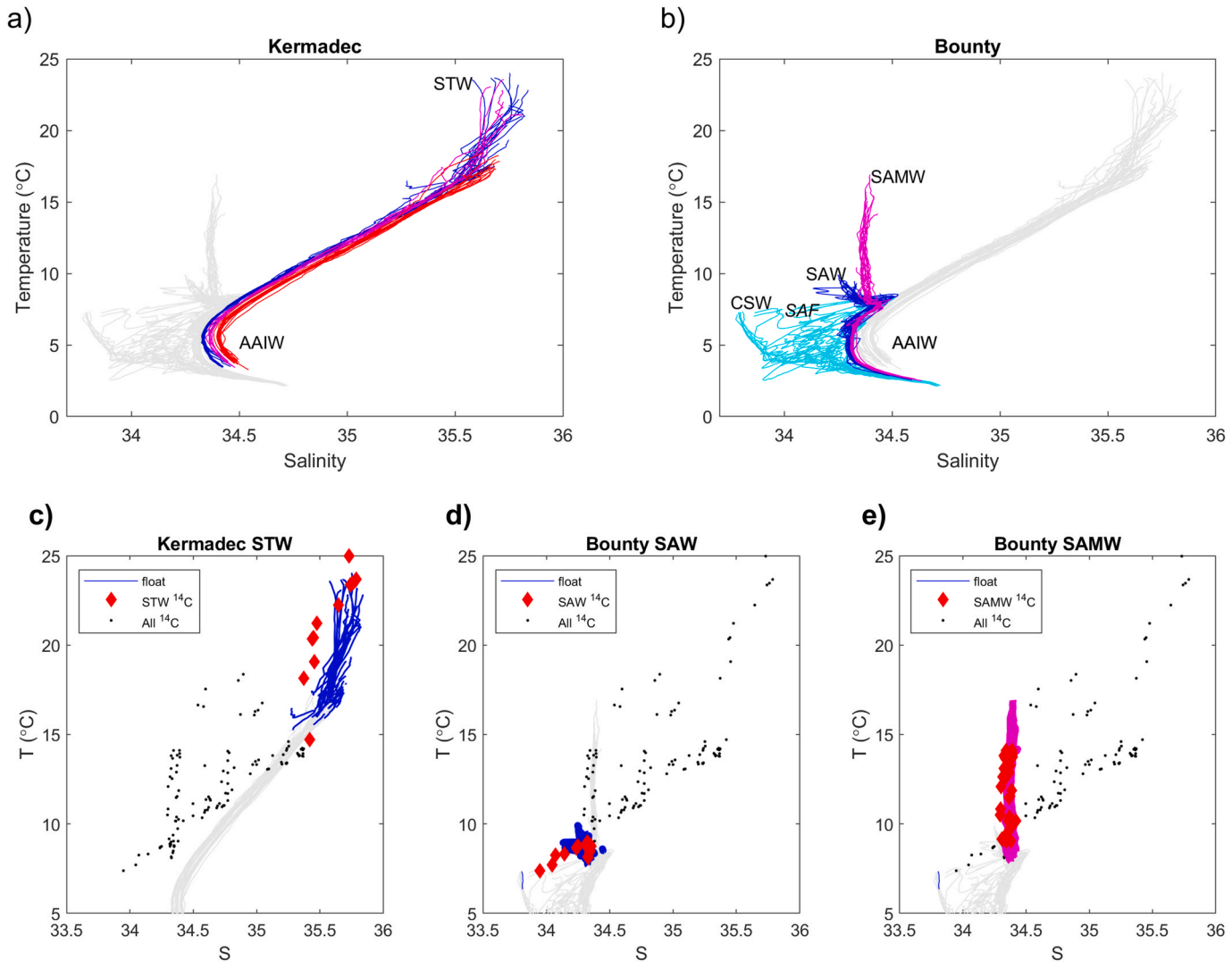

Fig. 2. Upper panels show temperature as a function of salinity (T–S) for profiles from the two floats. **a)** Kermadec float; and **b)** Bounty float. The colours indicate the locations of the profiles (see Fig. 1). In each case, the properties for the other float are shown in grey. Surface waters are Subtropical Water (STW), Subantarctic Mode Water (SAMW), Subantarctic Water (SAW), and Circumpolar Surface Water (CSW), while the intermediate water is Antarctic Intermediate Water (AAIW). Lower panels show T-S properties of surface waters where ^{14}C-uptake measurements were made (see Table 1). Black dots show T-S properties for all ^{14}C measurement sites. Filled red diamonds show T-S properties for sites used to tune NPP models, open red diamonds show STW sites not used in tuning. Blue or magenta lines show T-S properties from the upper 100 m of the float profiles (see Fig. 2); **c)** Kermadec float; **d)** Bounty float in SAW; and **e)** Bounty float in SAMW.

cleaned polycarbonate) incubated either *in situ* (using a free-drifting array drogued at 10 m), or in on-deck temperature-controlled incubators that simulated *in situ* irradiance levels. Before incubation, total added ^{14}C activity was assayed on triplicate controls containing ethanolamine to quantify initial radioactivity at each depth incubation. Each bottle was spiked with ^{14}C-bicarbonate (DHI, Denmark or PerkinElmer, USA). Samples were then filtered onto 0.2-µm pore-size 25/47-mm polycarbonate filters and kept frozen until analysis. Once on land, filters were acidified, Hi Safe 3 liquid scintillation cocktail was added and disintegrations per minute were then estimated using a scintillation counter following procedures described most recently in Gutiérrez-Rodríguez et al. (2020).

3. Results

3.1. Kermadec float, subtropical water

The Kermadec float, WMO 5905108, was deployed in July 2017 north-east of New Zealand. This float then travelled westwards from 175°W to 177°E, between 31°S and 35°S, with a short excursion up and down the Kermadec Ridge, which it crossed between L'Esperance and L'Havre Rocks (Fig. 1). The salinity sensor failed when the float was just east of Te Ika a Māui North Island in late October 2018.

Surface temperature for this float ranged between 17 °C and 24 °C, and salinity ranged between 35.5 and 35.8 (Fig. 2). Profiles from west of the ridge did not show the surface warming seen in the other profiles since they were taken in winter, but the surface temperature and salinity for all profiles were characteristic of STW in this region (Heath, 1985). Below the surface, salinity decreased until it reached a minimum in Antarctic Intermediate Water (AAIW) at about 1000 m depth (e.g., Bostock et al., 2013).

The air-sea heat flux (Q_f), PAR, temperature, and salinity from this float are shown in Fig. 3. PAR peaked in December (summer) and had a minimum in June (winter). Summer heating (negative Q_f) began in September of each year, and summer showed a warm, slightly more saline (due to evaporation) mixed layer of about 20 m depth (both MLD_{03} and MLD_{125}), with maximum SST of 24 °C in February. Ocean cooling began in March 2018, and the mixed layer deepened due to convective overturn to reach deepest values of about 100 m in June for MLD_{03}, and 200 m in August for MLD_{125}. Minimum SST was 17 °C in

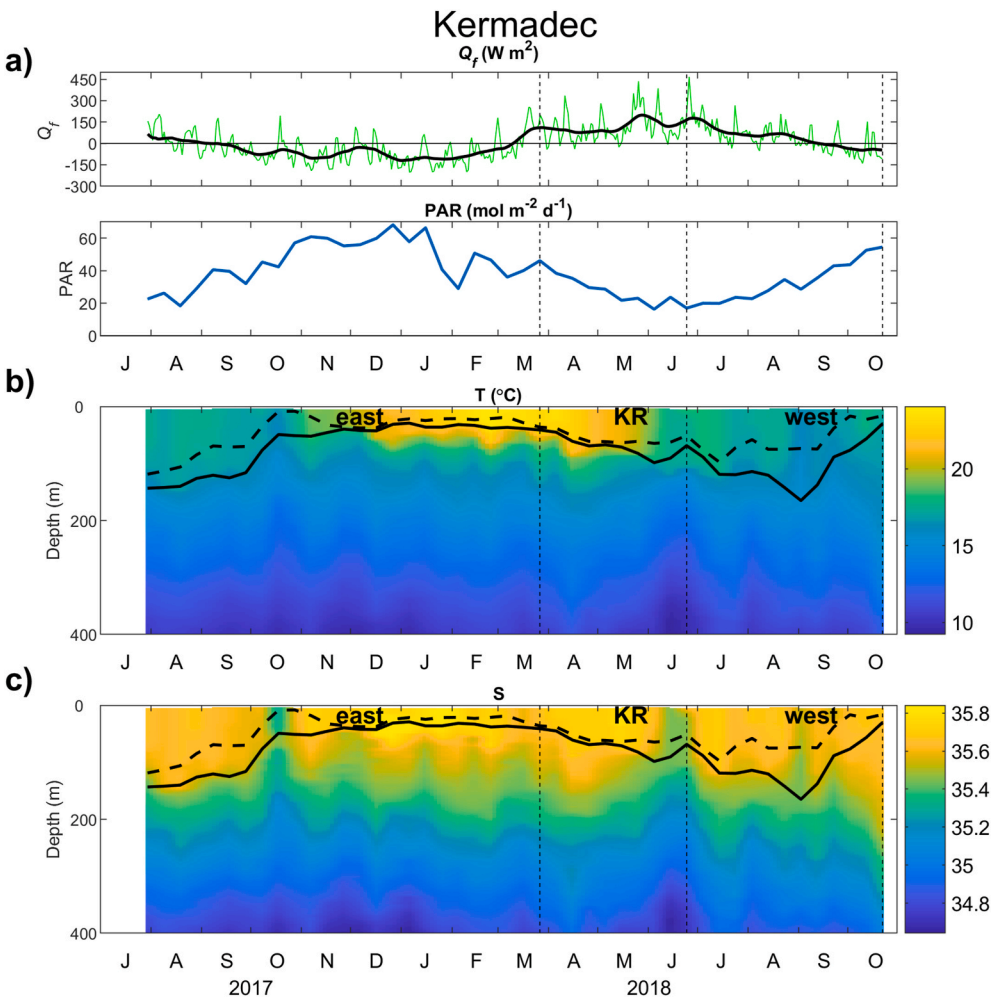

Fig. 3. Physical data for the Kermadec float. **a)** Air-sea heat flux (Q_f, green line) and smoothed with a one-month window (black line), and daily-mean photosynthetically active radiation (PAR) derived from MODIS satellite for the float locations; **b)** Temperature (T); and **c)** Salinity (S) from the float profiles. Dashed and solid black lines in b) and c) show the mixed layer depths, MLD_{03} and MLD_{125}, calculated using two different density criteria (see text). Labels 'east', 'KR' and 'west' indicate the float regimes (see Fig. 1 and text).

September or October, depending on the year, just before the heat flux changed sign, but about 2 months after the deepest MLD_{125}. Oscillations in isotherms, especially noticeable at about 200 m depth were likely due to internal tides.

The Kermadec float returned reasonably complete data for C_P and O_2, although NO_3 was missing for the latter third of the record, and much of the Chl record was missing above 80 m due to non-photochemical quenching (Fig. 4).

At these latitudes (35°–31°S), sea-surface chlorophyll has a minimum in summer and rises throughout winter, even as the mixed layer deepens, to reach a peak in September (Chiswell et al., 2013), and this pattern is seen in the MODIS observations of SSC (Fig. 4a). There were no near-surface chlorophyll (Chl_{10}) observations from the float in 2017, but in 2018, Chl_{10} rose throughout winter to reach 0.7 mg Chl m^{-3} in late spring (about double the satellite-based value).

The loss of data limits analysis of chlorophyll in the mixed layer. However, both winters were characterised by elevated carbon phytoplankton, C_P. The 2017 winter was followed by the development of a deep chlorophyll maximum (DCM) reaching 1 mg Chl m^{-3}, that was also a deep biomass maximum (Fig. 4a and b). This DCM initially appeared in October at a depth of about 50 m, just below MLD_{125}. The DCM deepened to a maximum depth of about 100 m in January, it then became more diffuse, but persisted until it was mixed upwards by deepening mixing in June. During the 10 months of available nitrate data, there was a strong nutricline between 100 and 200 m depth. Near-surface values of nitrate were low (~1.5 mmol m^{-3}) in October (spring), but increased by a factor of nearly two (to ~2.8 mmol m^{-3}) by April (autumn). Peak vertical nitrate gradients ($\partial NO_3/\partial z$) were 0.1 mmol m^{-3} m^{-1}, coincident with the DCM (not shown). Unfortunately, the NO_3 record was too short to determine if there was nitrate replenishment into the mixed layer in winter.

Oxygen had a deep oxygen maximum residing above the DCM, while the mixed layer was well ventilated during other times of the year.

Starting in March, both MLD_{03} and MLD_{125} deepened, and both Chl and C_P were well mixed down to MLD_{125}, indicating strong vertical overturn. After July, however, MLD_{03} started to shoal while MLD_{125} continued to deepen, and both Chl and C_P were only mixed to MLD_{03}. This suggests that during much of the winter, except for some sporadic instances, even when the seasonal thermocline was deepening, the rate of vertical overturn was not high enough to mix near-surface phytoplankton deeper than MLD_{03}. Similar results by Carranza et al. (2018) suggest that at these latitudes, plankton are well-mixed to the seasonal thermocline only during strong storms.

The chlorophyll to carbon ratio, [Chl:C_P], shows similar spatio-temporal patterns to Chl, with highest values of 0.04 (mg Chl:mg C_P) within the DCM in late summer (Fig. 5a).

Oxygen was at or near saturation levels in the mixed layer, except during winter overturn when the mixed layer oxygen was diluted by entrainment of lower-oxygen water from below the thermocline. The oxygen saturation anomaly ($\Delta O_2 = ([O_2 : O_{2sat}] - 1) \times 100$) reached 5% just above the DCM in summer (Fig. 5b). Since supersaturation at depth is an indicator of net photosynthetic production (e.g., Bushinsky and Emerson, 2015), this suggest positive net production just above the DCM in summer.

Near-surface biomass, C_{P10}, shows an annual cycle having a winter peak of 22.8 mg C m^{-3}, i.e. about 3 times the summer minimum of 7.4

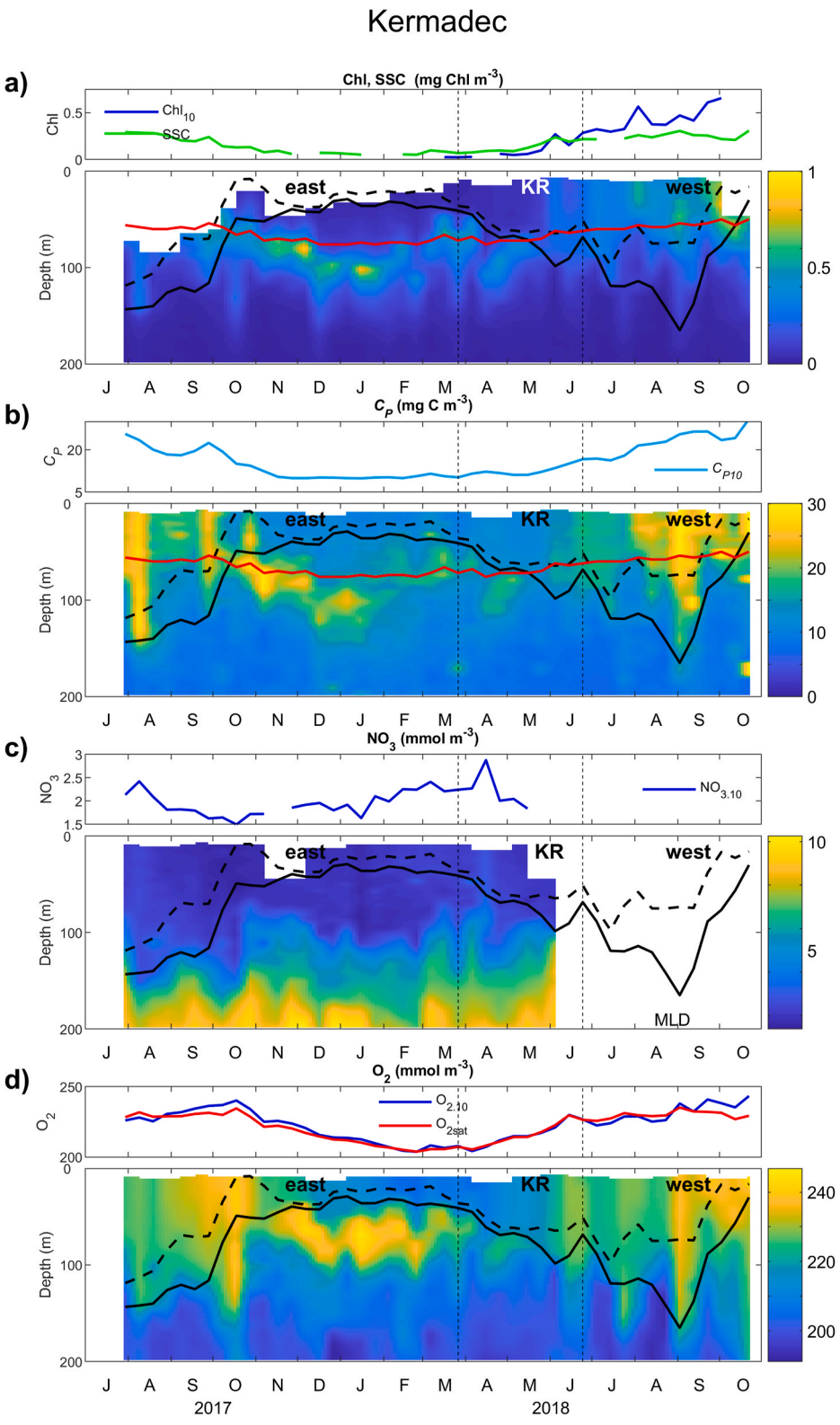

Fig. 4. Chlorophyll, phytoplankton carbon, nitrate, and oxygen for the Kermadec float. Panels show the near-surface (10 m depth) and section values. **a)** Chlorophyll (Chl), also shown is sea surface chlorophyll from the MODIS satellite (SSC, green); **b)** Phytoplankton carbon (C_P); **c)** Nitrate (NO_3); and **d)** Dissolved oxygen (O_2). Also shown are the mixed layer depths (MLD_{030} and MLD_{125}, black dashed and solid), and the 1% light level (I_{100}, red). Labels 'east', 'KR' and 'west' indicate the float regimes (see Fig. 1).

mg C m^{-3} (Fig. 5c). In comparison, the depth-integrated biomass, $C_{P0/300}$, has a much flatter annual cycle with its maximum (3500 mg C m^{-2}) only about 1.5 times its minimum value (2000 mg C m^{-2}). From mid-summer to late-autumn (January to May) depth-integrated biomass decreased (i.e., the accumulation rate, $r_{0/300}$, was negative), even though near-surface biomass levels increased ($r_{10} > 0$, Fig. 5d).

VGPM estimates of depth-integrated NPP have a mean value over the float duration of 440 mg C m^{-2} d^{-1} which is close to C_{P10} scaled by a factor of 30 m d^{-1} (Fig. 5e). This reflects the (Behrenfeld and Falkowski, 1997b) algorithm's strong dependence on surface chlorophyll.

3.2. *Bounty float, subantarctic waters*

The Bounty float, WMO 5904677, was deployed south of Tasmania

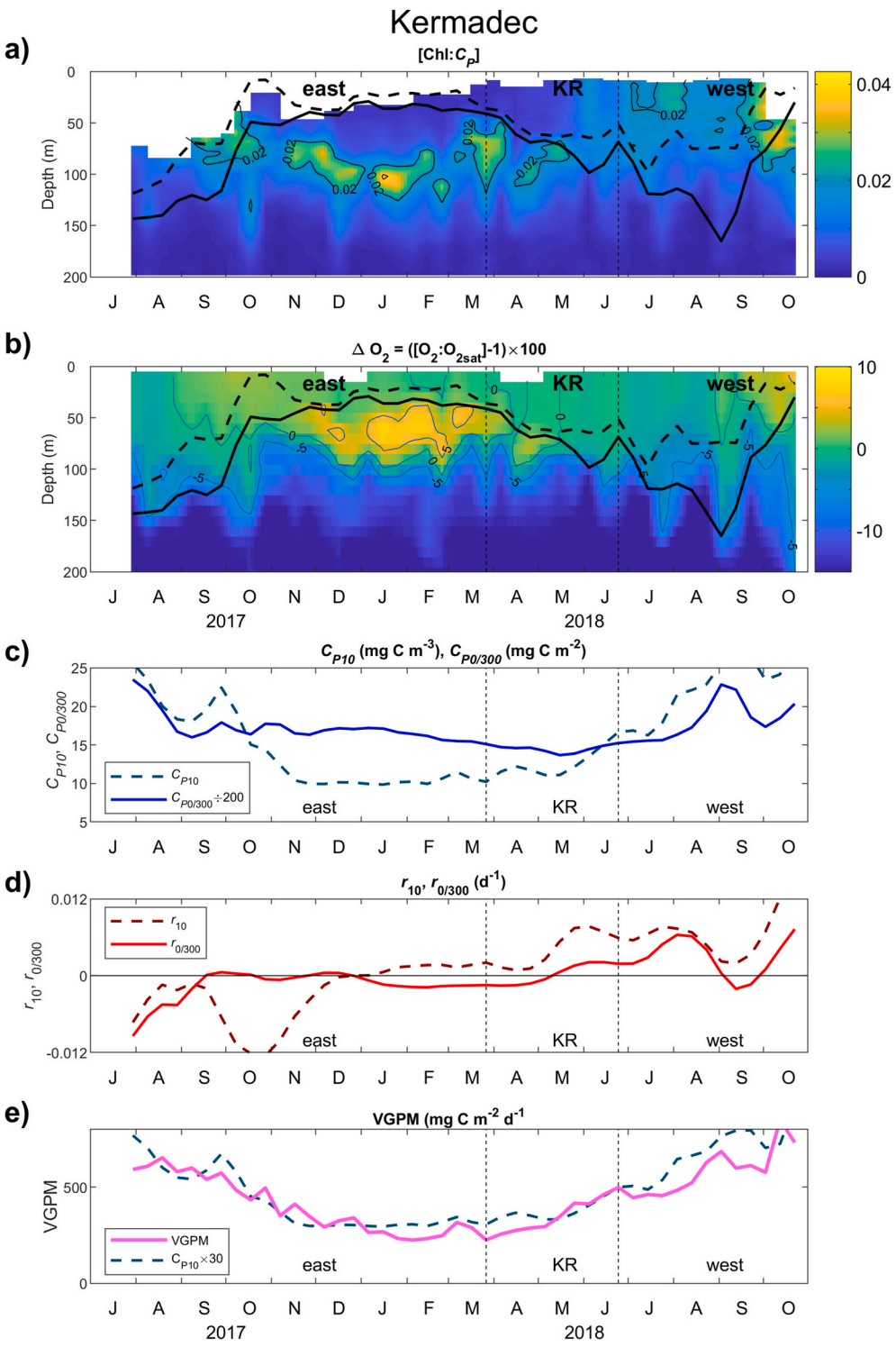

Fig. 5. Kermadec float derived quantities. **a)** Chlorophyll to phytoplankton carbon ratio [Chl:C_P]; **b)** Oxygen saturation anomaly ($\Delta O_2 = ([O_2 : O_{2sat}] - 1) \times 100$); **c)** Near-surface (10 m) and depth-integrated (0–300 m) phytoplankton carbon (C_{P10} and $C_{P0/300}$), $C_{P0/300}$ is scaled by 1/200; **d)** Specific accumulation rates ($r_{10} = \partial \ln C_{P10}/\partial t$ and $r_{0/300} = \partial \ln C_{P0/300}/\partial t$) for near-surface and depth-integrated phytoplankton carbon, respectively; and **e)** Depth-integrated net primary production from the Vertically-Generalised Production Model (VGPM, magenta), with C_{P10} multiplied by 30. Also shown in a) and b) are the mixed layer depths (MLD_{030} and MLD_{125}, black dashed and solid).

in April 2016 (Fig. 1). T-S properties (Fig. 2b) show that the float passed through three distinct water mass regimes. It was deployed in a region of slow flow within Circumpolar Surface Water, it then became entrained in the Subantarctic Front (SAF) and for the next 9 months travelled eastwards in the SAF where the surface waters were mixed between Circumpolar Surface Water and SAW. In 2017 the float drifted along the eastern flank of the Campbell Plateau and into the Bounty Trough where surface water was SAW. In October 2018, while still in the Bounty Trough it transitioned into warmer water that had surface salinity of 34.35–34.4, which is characteristic of Subantarctic Mode Water (SAMW, Morris et al., 2001), although its temperature was higher than typically associated with SAMW. This elevated temperature was almost certainly due to the extensive 2017/2018 marine heat wave seen around New Zealand at that time which showed temperature anomalies as high as 0.5–0.8 °C in the Bounty Trough during January 2018 (Salinger et al., 2019; see their Fig. 3).

We denote the three flow regimes encountered by this float as SAF, SAW and SAMW, respectively. The SAF regime exhibits deep winter mixing exceeding 400 m, with considerable temperature and salinity variability, presumably due to relative movement of the float across the

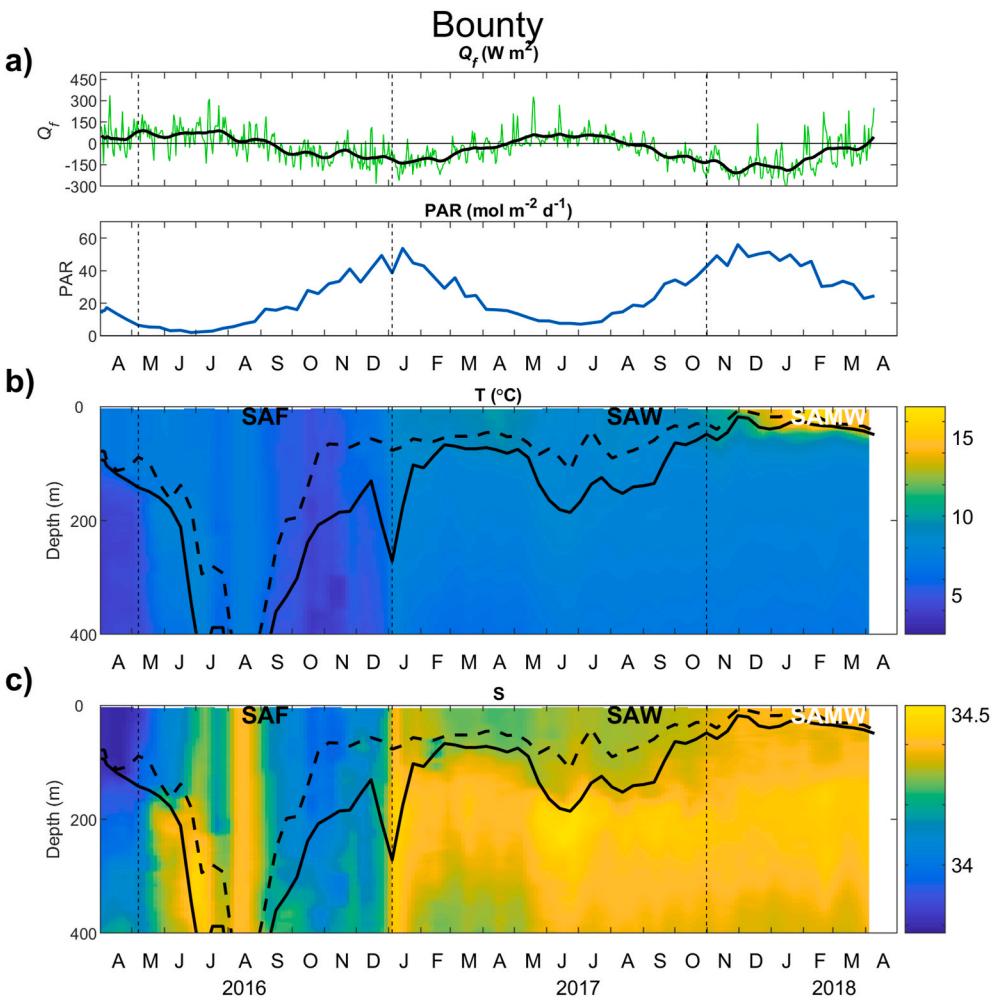

Fig. 6. Physical data for the Bounty float. **a)** Air-sea heat flux (Q_f, green line) and smoothed with a one-month window (black line), and daily-mean photosynthetically active radiation (PAR) derived from the MODIS satellite for the float locations; **b)** Temperature (T); and **c)** Salinity (S) from the float profiles. Dashed and solid black lines in b) and c) show the mixed layer depths, MLD_{03} and MLD_{125}, calculated using two different density criteria (see text). Labels 'SAF', 'SAW', and 'SAMW' indicate the float regimes (see Fig. 1).

frontal zone (Fig. 6). In the SAW regime, SST was 10 °C in summer and 8.5 °C in winter, while summer and winter MLD_{125} were 70 m and 200 m, respectively. The transition to SAMW was marked by shallower mixed-layer depths of ~40 m.

Chlorophyll data were mostly missing above 100 m because of non-photochemical quenching (Fig. 7), and at these high latitudes SSC from MODIS was also often missing due to cloud cover. Where both quantities exist, Chl_{10} was generally higher than SSC by a factor of 2 or more.

Both C_P and Chl (where available) indicate low phytoplankton concentration in the SAF regime, and spring or summer blooms in SAW and SAMW that terminated at about the time the mixed layer started to deepen in early autumn. The missing chlorophyll data make it uncertain whether there was a summer DCM in SAW, although there is a suggestion of elevated C_P at the base of the mixed layer in March and April 2017 (autumn, Fig. 7b). In SAMW, both Chl and C_P show limited evidence of weak maxima at about 40 m depth.

In the SAF regime, NO_3 and O_2 co-vary and reflect the aliasing as the float traversed strong physical and chemical gradients across the front, so that paradoxically, NO_3 showed lowest concentrations during winter deep mixing and highest values during the spring. Within the SAW regime, NO_3 was generally lower within the mixed layer than at depth, but still exceeded 14 mmol m^{-3}. There is slight evidence of replenishment during winter mixing in 2017, when mixed-layer concentrations rose (although near-surface levels did not change substantially). There was subsequent drawdown during the following production phase. In the SAMW regime, both NO_3 and O_2 were depleted in the mixed layer compared to the SAW regime (to 5.5 and 240 mmol m^{-3}, respectively).

Interpretation of [Chl:C_P] for this float is complicated by missing chlorophyll data (Fig. 8a), but in both SAW and SAMW, [Chl:C_P] was highest from February to May, i.e., after the summer production (Fig. 8).

Oxygen in the mixed layer was well ventilated at all times, with the oxygen saturation anomaly, ΔO_2, typically near zero, although ΔO_2 increased to ~5% associated with the increase in primary production when the float transitioned into SAMW.

The lack of a strong deep biomass maximum at these southern latitudes means that $C_{P0/300}$ followed C_{P10} well in all of these southern water masses (Fig. 8c), hence the near-surface and depth-integrated specific accumulation rates are essentially the same (Fig. 8d).

VGPM estimates for this float have mean values of 316 and 760 mg C m^{-2} d^{-1} in SAW and SAM, respectively. In SAW, the VGPM algorithm produces an estimate of depth-integrated NPP that is nearly proportional to the surface phytoplankton biomass, C_{P10}, scaled by a factor of 15 m d^{-1}. In SAMW, this proportionality breaks down due to the anomalously high temperature seen at the end of the float deployment (Salinger et al., 2019).

4. NPP models

A total of 131 ^{14}C-uptake measurements of net primary production, made mostly east of New Zealand were available to tune the models (Fig. 1, Table S1). Each model was tuned separately for each float using NPP measurements from sites where the surface T-S properties were close to, or within the envelope, of T-S properties from the respective float profiles (Fig. 2c, d, e).

Model 1 was tuned by choosing ν_1 to minimise the root-mean-square differences between model estimates and NPP observations for the

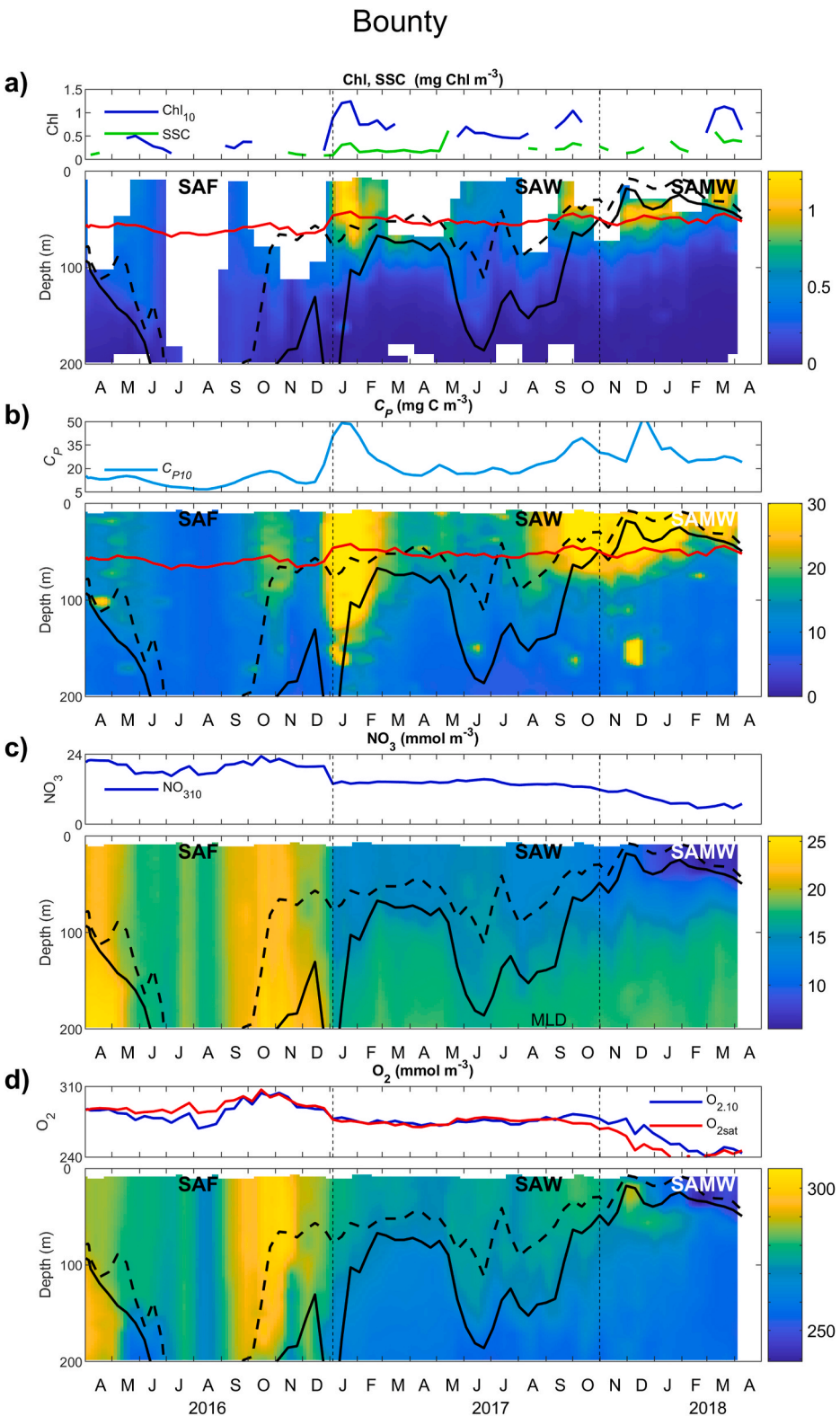

Fig. 7. Chlorophyll, phytoplankton carbon, nitrate, and oxygen for the Bounty float. Panels show the near-surface (10 m depth) and section values. **a)** Chlorophyll (Chl), also shown is sea surface chlorophyll from the MODIS satellite (SSC, green); **b)** Phytoplankton carbon (C_P); **c)** Nitrate (NO_3); and **d)** Dissolved oxygen (O_2). Also shown are the mixed layer depths (MLD_{030} and MLD_{125}, black dashed and solid), and the 1% light level (I_{100}, red). Labels 'SAF', 'SAW', and 'SAMW' indicate the float regimes (see Fig. 1).

respective days of the year. Model 2 was tuned similarly by choosing ν_2 for various n (see Supporting Information for details). The results were not very sensitive to the choice of n, but best results were obtained with $n = 1$ for both floats (Table 1), suggesting that the response to light is shallower and not as flat as the Behrenfeld et al. (2005) equation would suggest (see Supporting Information).

Fig. 9 summarises how NPP from the tuned models compares with the ^{14}C-uptake measurements for all three water masses. The ^{14}C-uptake measurements were mostly made in summer/autumn (February to April) or spring (September and October), and hence cannot capture the annual cycles of primary production. In particular, there are no ^{14}C-uptake measurements for winter for either float. In STW, Model 1 tends to fit the observations better in the upper 50 m, whereas Model 2 tends to fit better below 50 m. For the four months that have observations,

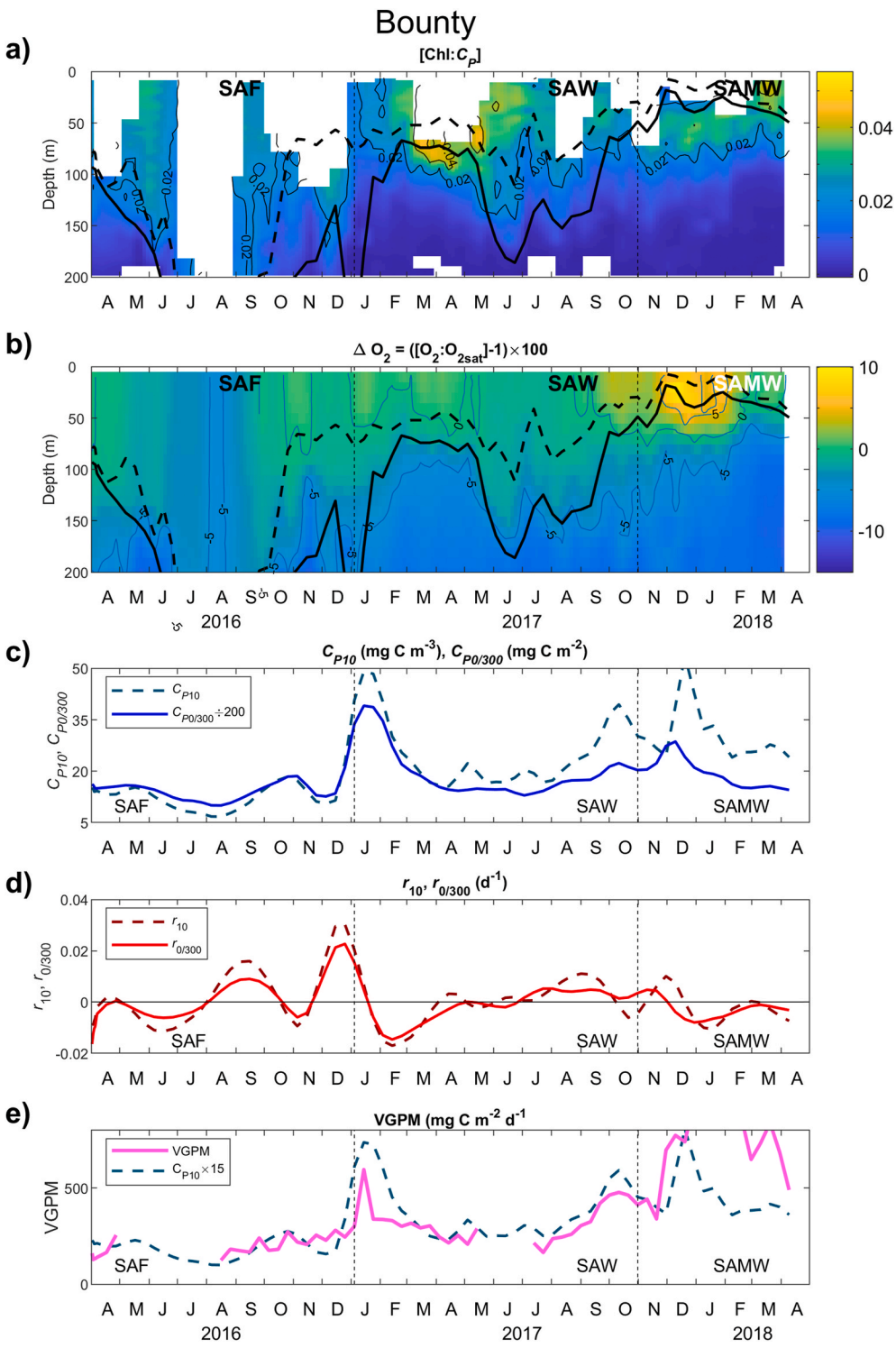

Fig. 8. Bounty float derived quantities. **a)** Chlorophyll to phytoplankton carbon ratio, [Chl:C_P]; **b)** Oxygen saturation anomaly ($\Delta O_2 = ([O_2 : O_{2sat}] - 1) \times 100$); **c)** Near-surface (10 m) and depth-integrated (0–300 m) phytoplankton carbon (C_{P10} and $C_{P0/300}$), $C_{P0/300}$ is scaled by 1/200; **d)** Specific accumulation rates ($r_{10} = \partial \ln C_{P10}/\partial t$ and $r_{0/300} = \partial \ln C_{P0/300}/\partial t$) for near-surface and depth-integrated phytoplankton carbon, respectively; and **e)** Depth-integrated net primary production from the Vertically-Generalised Production Model (VGPM, magenta) with C_{P10} multiplied by 15. Also shown are the mixed-layer depths (MLD_{030} and MLD_{125}, black dashed and solid).

Model 1 returns better scores in February and April, whereas Model 2 does better in March and September. For SAMW, there is substantial production deeper than about 25 m that is not captured by Model 1, and Model 2 tends to underestimate production above 25 m. Model 2 scores better each month except November.

Fig. 10 shows the annual cycles of depth-integrated NPP, NPP_{int}, from both models and VGPM for each water mass, along with depth-integrated NPP from the ^{14}C uptake measurements. For STW, the model tuning is hampered by a lack of ^{14}C uptake measurements outside of February–April. Two values of depth-integrated NPP from February and March were well outside the range of other estimates of depth-integrated NPP for these months, and were not used in the model tuning (shown as open diamonds). One high observation in October was from a site near the highly productive STF which possibly should not be included in the calibration, but since both models show peaks at this time, this measurement was included.

VGPM estimates for this float are about half the ^{14}C-uptake values, and given the large separation between the float trajectory and the ^{14}C-uptake sampling sites, we investigated the possibility that this discrepancy could be due to spatial differences in VGPM. However, VGPM

Table 1
Model scores.

	STW, Kermadec 13 profiles		SAW, Bounty 19 profiles		SAMW, Bounty 28 profiles	
	Mean	RMS	Mean	RMS	Mean	RMS
Model 1	**81**	**232**	**106**	**232**	**3**	**150**
Model 2, n = 0.5	165	222	149	237	95	167
Model 2, n = 1	**−12**	**142**	**92**	**209**	**32**	**141**
Model 2, n = 2	−200	244	30	194	−36	142
Model 2, n = 3	−294	326	0	193	−68	153
Model 2, n = 5	−390	416	−31	196	−100	170
VGPM	**382**	**436**	**8**	**275**	**−124**	**234**

Model scores (mg C m^{-2} d^{-1}), defined as the mean and root-mean-square of the difference between modelled and observed ^{14}C-uptake estimates of depth-integrated net primary production (NPP) at corresponding days of the year. Model 1 and VGPM have no tuneable parameters, Model 2 has been tuned by choosing the value of n to minimise the model score (see Supporting Information). Bold values are for the models used in this article.

estimates for the ^{14}C-uptake measurement sites are consistent with VGPM estimates at the float locations, indicating that the discrepancy is more likely to be due to real differences between VGPM and ^{14}C-uptake values.

For SAW, both models and VGPM suggest depth-integrated NPP, NPP_{int}, peaks in January/February. For SAMW, VGPM values were much higher than the ^{14}C-uptake measurements, but since these are coincident with the 2017/18 marine heat wave (Fig. 10a), we suspect this reflects a sensitive temperature dependence in the VGPM algorithm.

Timeseries of modelled NPP (Fig. 11), and depth-integrated NPP and losses (Fig. 12), illustrate the depth- and temporal-differences between the models. For STW, both models suggest NPP is low over summer and autumn, but peaks in late spring. Primary production is predominately near the surface from July to October, but the DCM contributes a sizeable fraction of NPP_{int} from November to June – as much as 60% of NPP_{int} in Model 1, and as much as 90% in Model 2 (Fig. 12a). For SAW and SAMW, both models suggest NPP is low throughout winter, but rises in spring and peaks in summer. Model 1 suggests production is almost entirely within the upper 50 m, although Model 2 suggests production below 50 m reaches 50% of the total during November and December.

The depth-integrated losses, L_i, closely match NPP_{int} for both models in all water masses, suggesting a high degree of coupling between production and losses. Both models show near zero lag between losses and production for STW. In SAMW and SAW, losses lag NPP by ~10 d for Model 1 and by ~15 d for Model 2.

5. Discussion

On average the BGC-Argo float-derived estimate of near-surface chlorophyll (where available) was 20% higher than the satellite-derived estimate of sea surface chlorophyll for the Kermadec float and 3 times as high for the Bounty float. While some of this mismatch reflects the fact that float values are point measurements from below the surface whereas the satellite data are 9-km 8-d composites derived from ocean colour, and that the relationship between fluorescence and chlorophyll concentration could vary with latitude due to differences in light, nutrients, and/or phytoplankton physiology (e.g., Claustre et al., 2020), it may also be that the BGC-Argo fluorometer calibrations were in error.

There is some evidence that BGC-Argo floats could have a systematic bias towards overestimating fluorescence. Roesler et al. (2017) made a

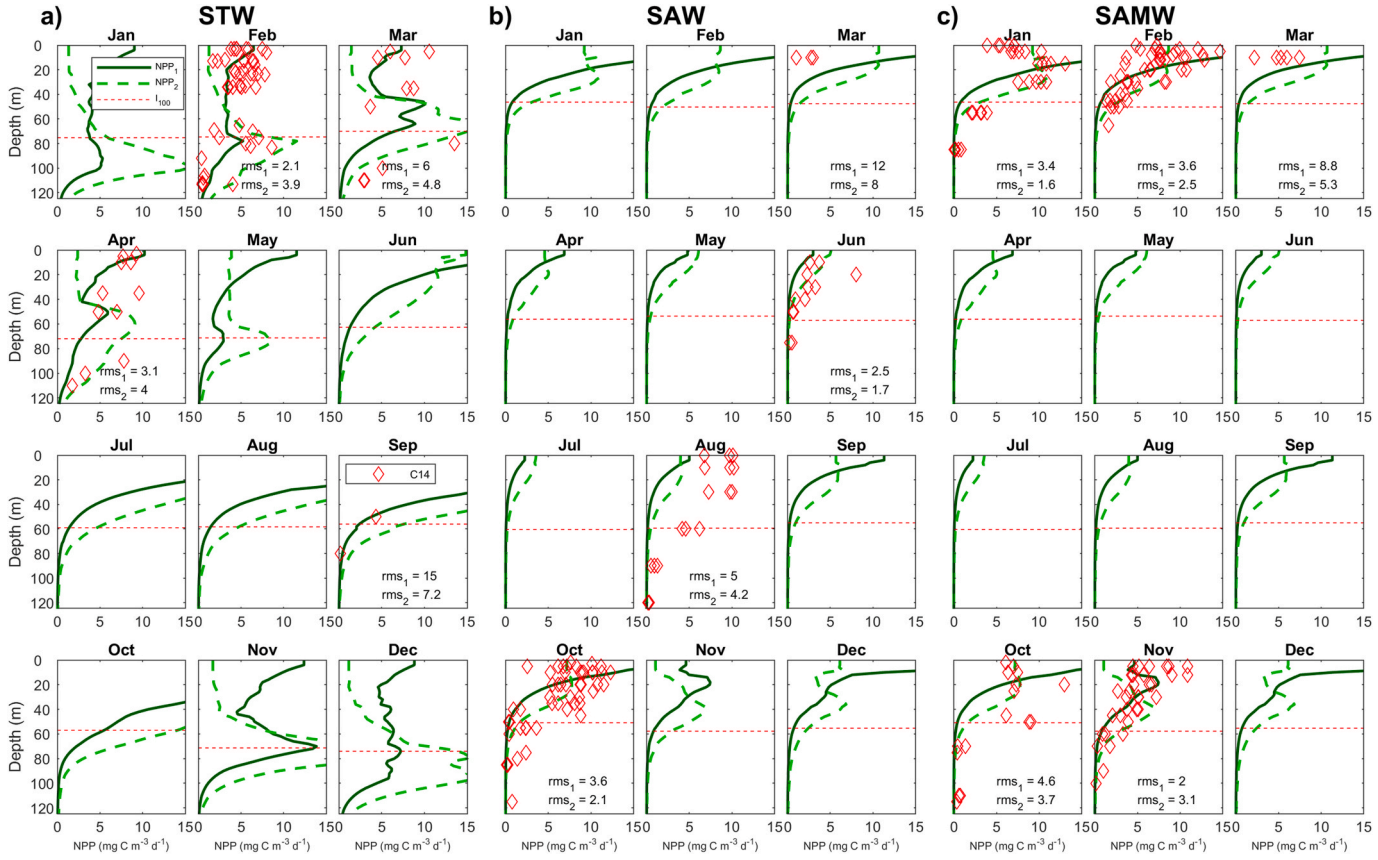

Fig. 9. Net primary production as function of depth from the two models and ^{14}C-uptake measurements for **a)** Subtropical water (STW); **b)** Subantarctic water (SAW); and **c)** Subantarctic mode water (SAMW). The ^{14}C-uptake measurements (red diamonds) have been grouped by month of the year. The net primary production for Model 1 (NPP_1, dark green) and Model 2 (NPP_2, dashed light green) have been averaged over the respective months of the year. Locations of the ^{14}C-uptake measurements are shown in Fig. 1. Root-mean-square differences (rms) between model and observed primary production are shown for each model.

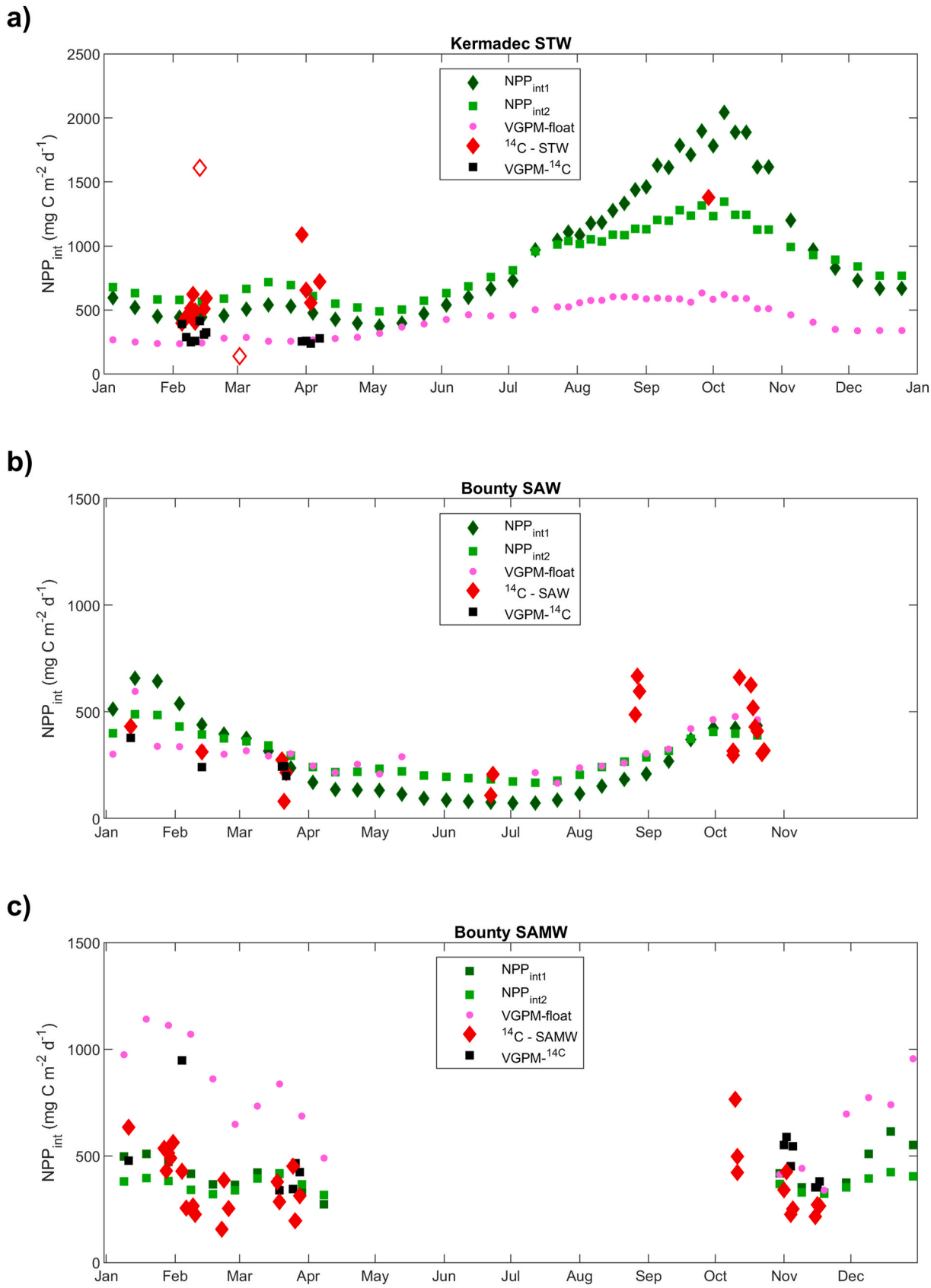

Fig. 10. Depth-integrated net primary production (NPP_{int}) along the float tracks as a function of year day from models, NPP_{int1} (dark green diamonds), NPP_{int2} (light green squares), and VGPM (magenta dots). Also shown are ^{14}C-uptake measurements of NPP_{int} for the respective water masses (red diamonds) with data used for model tuning shown as filled diamonds. VGPM estimates of NPP_{int} at the ^{14}C-uptake measurement sites are shown as black squares. **a)** Kermadec float in STW; **b)** Bounty float in SAW; and **c)** Bounty float in SAMW.

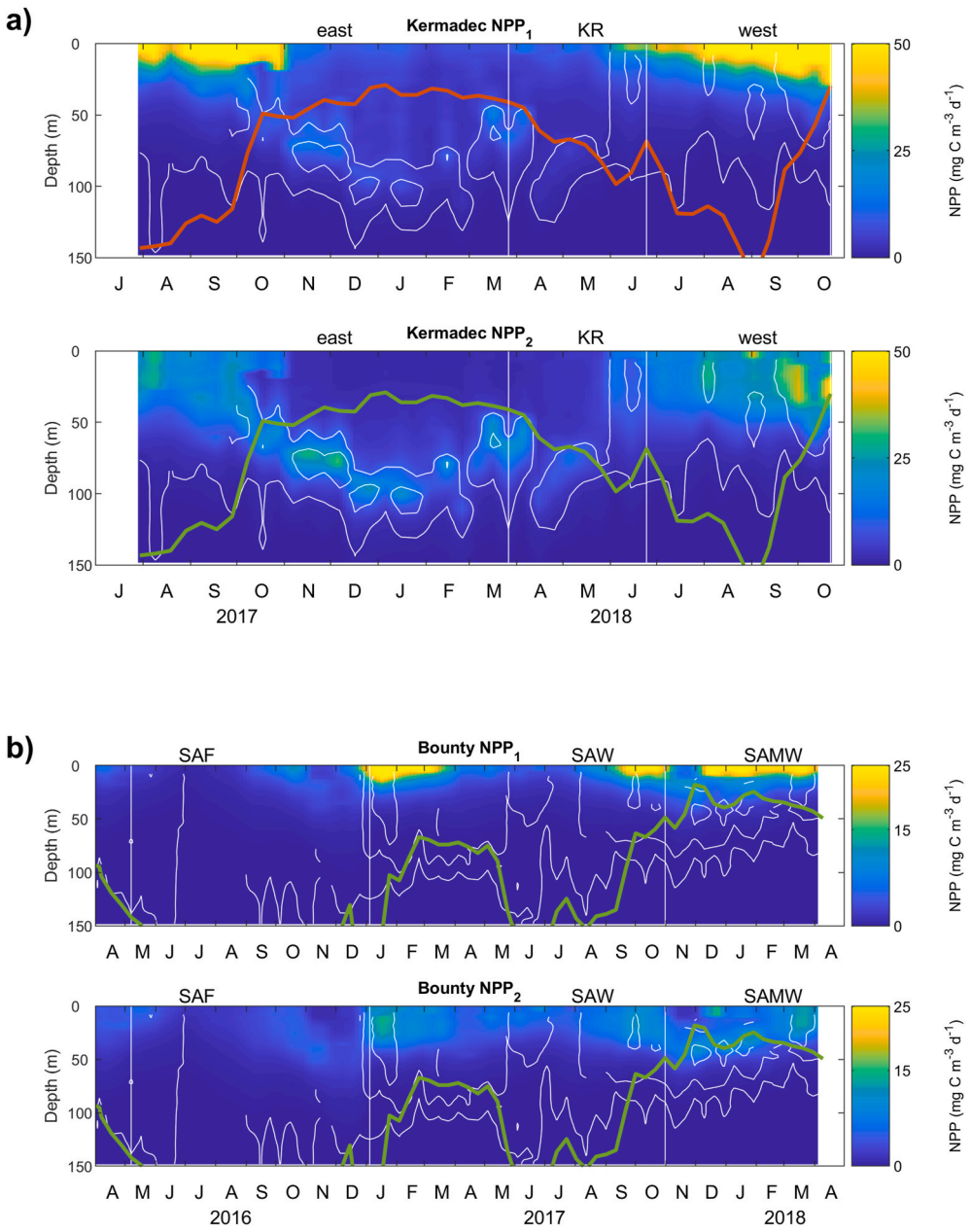

Fig. 11. Modelled primary production from the two models (NPP_1 and NPP_2) for **a)** Kermadec float; and **b)** Bounty float. In each case, the red line is mixed-layer depth (MLD_{125}), and white lines are contours of chlorophyll (see Fig. 4 and 7).

global analysis of WET Labs ECO sensors (used in both floats) and recommend a factor of 2 correction be applied at the user level, although this may be limited to the Southern Oceans because Xing et al. (2011) shows good correlation for global data. Phung (2020) found better results from data taken around New Zealand, but still found BGC Argo surface chlorophyll values were ~27% higher than the satellite values.

Given that we only used data from one float in each water mass, miscalibrations of individual floats would not be a serious issue. If the chlorophyll values for either float were out by a simple scaling factor, our values of Chl and [Chl:Cp], and subsequently ν_1 and ν_2 would also out by the same scaling factor, but since the models were tuned against observations, there would be no difference to the estimated values of NPP or losses, and none of our conclusions would be altered.

A bigger problem would be if float fluorometer calibrations drifted throughout the float deployments, for example due to biofouling or instrument degradation. There is some evidence of calibration drift since the ratio of satellite to float-based measurements of chlorophyll changed over the float deployments from ~1 to ~3 for the Kermadec float (Fig. 4a) and from ~4 to ~2 for the Bounty float (Fig. 7a). Unfortunately, we do not have independent estimates of fluorescence to determine if these ratio changes are due to fluorometer calibration shifts or reflect variable real-ocean fluorescence to ocean colour ratios. Given the relatively small overlap between satellite and BGC-Argo data and that the drifts were in opposite directions for each float, it would be unwarranted to calibrate the float chlorophyll against satellite chlorophyll. However, if the float fluorometers did drift as implied by the changes in this ratio, then chlorophyll (and hence NPP) would be relatively overestimated by a factor as much as 3 towards the end of the Kermadec deployment, and relatively underestimated by a factor as much as 2 towards the end of the Bounty deployment. A comparison of BGC-Argo fluorescence is well beyond the scope of this article, and we flag this as a potential issue for the community.

Because of their sampling strategy, BGC-Argo floats provide quasi-Lagrangian observations (i.e., they do not exactly follow a particular

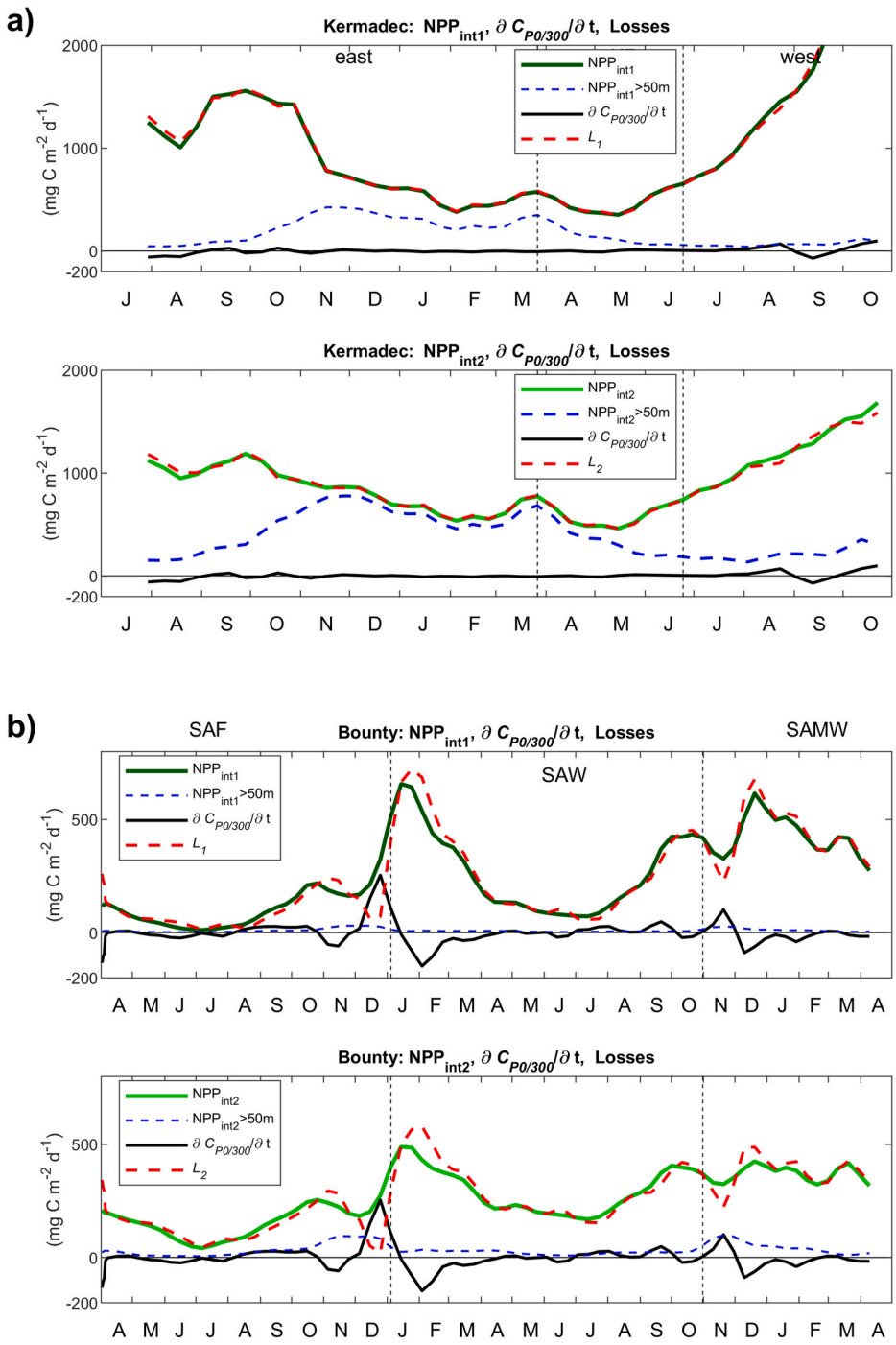

Fig. 12. Modelled depth-integrated net primary production and depth-integrated losses from the two models for **a)** Kermadec float; and **b)** Bounty float. Panels show depth-integrated NPP from the models (NPP_{int1}, NPP_{int2}, green lines), the contribution to NPP_{int} from below 50 m (blue dashed lines), depth-integrated growth ($\partial C_{P_{0/300}}/\partial t$, black lines), and depth-integrated losses (L, red dashed lines). Labels 'east', 'KR', 'west', 'SAF', 'SAW', and 'SAMW' indicate the float regimes (see Fig. 1).

water parcel), and by treating the observations as Eulerian we have implicitly assumed that the water masses are homogeneous biomes. This may not always be the case, for example, the timing of the annual peak in surface chlorophyll in STW varies with latitude (Chiswell et al., 2013). In addition, with float deployments of 14, 10 and 5 months in STW, SAW, and SAMW, respectively, the descriptions of annual cycles have low statistical significance. Nevertheless, these float data provide the only available continuous observations of these biogeochemical quantities in these water masses, and so provide qualitative if not quantitative estimates of the seasonal cycles.

For the same reasons, the models provide fits to the data along the float trajectories rather than homogeneous biomes. Apart from the potential fluorometer drift and the loss of chlorophyll data due to non-photochemical quenching (particularly for the Kermadec float), perhaps the biggest limitation of the models is that they assume constant values of ν_1 and ν_2, thus the specific production rates are a function of light only and neglect the complex nutrient, light, temperature, and species dependencies of production (e.g., Barton and Yvon-Durocher, 2019; Laws, 2013).

As one might expect, given the simplicity of the models, neither model perfectly simulates the vertical structure of primary production. For STW, Model 1 tends to simulate the near-surface production better,

and Model 2 tends to simulate the deep production better (Fig. S3), so that quite possibly a different formulation of the light parameterization might lead to better simulations. For SAW/SAMW, Model 2 generally performs better than Model 1 throughout the water column. Both models, however, suggest a substantial fraction of primary production occurs at depth in STW, which is corroborated by the ^{14}C-uptake measurements (Fig. S3) and CTD fluorescence profiles showing deep chlorophyll maxima (Nodder et al., 2016, their Fig. 7).

The model tuning unavoidably was made by fitting the models to spatially sparse and temporally non-concurrent, data. The spatial mismatch between float locations and ^{14}C-uptake measurement sites for STW was considerable (the closest distance between float and ^{14}C-uptake measurement site was ~1100 km), so that the tuning may have considerable error for this site. However, even if NPP_{int1} and NPP_{int2} for STW were wrong by a factor or 2 or 3 (so that they matched VGPM), the models would still point to the importance of subsurface production, to the timing of the blooms, and to increasing stability of the water column as the controlling force of the production in STW. For the southern water masses (SAW, SAMW), the ^{14}C-uptake measurements are dense enough that both models fall within the envelope of ^{14}C-measurements, and the uncertainty is less.

The seasonal cycle of STW production, based on the Kermadec float data (Fig. 4), is similar to that described for STW by Chiswell et al. (2015). Starting in summer, a strong thermocline provides a barrier to nutrient supply into the shallow surface mixed layer. Any nutrients remaining in the mixed layer from the previous winter are consumed. This leads to a low biomass phytoplankton community in the summer mixed layer, likely dominated by small phytoplankton cells (Ellwood et al., 2013), and sustained by bacterial and grazing-mediated nutrient recycling (Goldman et al., 1979; Laws, 2013). A DCM appears below the mixed layer, and because both C_P and [Chl:C_P] show deep maxima, and because oxygen is supersaturated just above it, the DCM appears to be a product of both photoacclimation and biomass accumulation. As the summer progresses and light levels increase, the DCM and the nutricline deepen because nutrients are consumed from the top of the nutricline (e.g. Wolf and Woods, 1988). After the change to ocean cooling in autumn, convective overturn deepens the mixed layer. At first this mixes up the DCM but then mixing reaches the nutricline, at which point, nutrients are entrained into the mixed layer. If there is sufficient winter light at these lower latitudes, this supports new production throughout the mixed layer during winter. NPP decreases in spring as decreasing vertical mixing reduces the supply of nutrients into the mixed layer, and eventually emerging stratification leads to summer conditions.

Because of the failure of the NO_3 sensor on the Kermadec float in June 2018, we did not observe replenishment of NO_3 due to deep mixing in winter, but mixed-layer NO_3 values during the winter of 2017 were not much higher than in summer (2.5 vs 1.5 mmol m^{-3}, Fig. 4c), as was also seen by Johnson et al. (2017b) for STW/STF water east of New Zealand. This suggests that nutrients are rapidly taken up as soon as they enter the mixed layer, and the production of phytoplankton is sustained by rapid remineralization (e.g., Laws, 2013). It is likely that production in these oligotrophic waters is nutrient limited even during winter. It is worth pointing out, that dissolved iron in STW mixed layers is low (Ellwood et al., 2008, 2018) and may be limiting production, rather than NO_3, but this does not impact the seasonal cycles.

One issue with this description of the STW seasonal cycle is that we saw an increase in mixed-layer NO_3 during the 2017/18 summer, when mixed layer nutrients should have been decreasing (Fig. 4c). It has been suggested that breaking internal waves (such as those responsible for the vertical displacements of isotherms, Fig. 3), could also inject nutrients into the mixed layer (Stevens et al., 2012) even in summer, but we speculate the main reason for this increase may be due to influences of topography (e.g., Priede et al., 2013) as the float approached the Kermadec Ridge, This points to one of the problems of trying to interpret Lagrangian float data in an Eulerian sense, where real spatial gradients in measured quantities can be falsely interpreted as temporal changes.

Both models are consistent with this STW seasonal cycle. However, even though they are tuned against the same ^{14}C-uptake measurements, the range of NPP_{int2} is about half the range in NPP_{int1} (~1200 vs 2500 mg C m^{-2} d^{-1}, Fig. 10). This is a consequence of the light function in Model 2 that shifts production deeper in the water column compared to Model 1, particularly in summer. Both models show a substantial contribution to depth-integrated NPP from the DCM, suggesting that between November and April at least 60%, and perhaps as much as 90%, of NPP_{int} occurs in the DCM. Since VGPM is effectively a rescaling of near-surface chlorophyll, it tends to underestimate this deep contribution to NPP.

For the Bounty float, SAW and SAMW were treated as different water masses because of the large increase in temperature, and decreases in nitrate and oxygen in the mixed layer in October 2017 (Figs. 6 and 7), even though the increase in temperature was a result of the 2017/2018 marine heat wave (Salinger et al., 2019; see their Fig. 3). SAMW is recognised as a distinct water mass found year-round over the Campbell Plateau (Morris et al., 2001), where both satellite imagery (Banse and English, 1997; Boyd et al., 2004) and *in situ* observations show higher production and phytoplankton biomass accumulation than surrounding waters (Gutiérrez-Rodríguez et al., 2020; Heath and Bradford, 1980).

SAW is recognised as high-nitrate low-chlorophyll (HNLC) and iron-limited water, although light and silicate can also become limiting at times (Boyd et al., 1999; Dugdale et al., 1995; Peloquin et al., 2011; Rintoul and Trull, 2001). Even during winter deep mixing, iron concentrations remain extremely low (and possibly limiting), with most iron thought to be supplied via Ekman transport from the south (Ellwood et al., 2008). In SAW, the ocean cooled until August, but the mixed layer reached its deepest level ~2 months earlier (in June), after which both MLD_{03} and MLD_{125} slowly shoaled. Both C_{P10} and $C_{P0/300}$ increased during this time (i.e. r_{10} and $r_{0/300}$ were positive). Thus, for SAW (and likely SAMW) there is net accumulation of biomass even in late winter (from June to October). That the mixed layer reaches its deepest before convective overturn ceases indicates that for the last 2–3 months of winter, convective overturn was not forming sufficient cool water to overcome erosion and hence shoaling of the thermocline due to internal mixing, and the ocean enters the low-turbulence regime discussed by Chiswell et al. (2015).

SAMW mixed-layers exhibited nitrate (Fig. 2) concentrations about one-half of those in SAW (7 compared to 17 mmol m^{-3}), while C_{P10} values were comparable with those of SAW, perhaps reflecting iron limitation in both water masses (Boyd et al., 1999).

For the Bounty float, the two models are consistent with the ^{14}C-uptake measurements, and depict near-identical representations of the annual cycles of production in SAW and SAMW (Fig. 10). Both models exhibit the seasonal cycles described above, with production confined to the upper mixed layer (although deeper in Model 2), and with production starting to increase as vertical convective overturn slows, but before the ocean starts to warm. In both models, production decreases once PAR starts to decrease, and deep chlorophyll maxima play less important roles in these water masses than further north. VGPM is also indistinguishable from the ^{14}C-uptake measurements for SAW, but showed a temperature response to the 2017/2018 marine heat wave in SAMW.

For all water masses and both models, the calculated depth-integrated loss rates (L in Fig. 12) almost exactly balance NPP, suggesting tight coupling between production and losses. The lag for STW was too small to determine, but for SAW and SAMW, the lag was 10 d lag for Model 1 and 15 d for Model 2. Phytoplankton growth and micro-zooplankton grazing rates have different temperature dependencies (Banse, 1982; Rose and Caron, 2007), and this lag suggests that a stronger temperature dependence for grazing limit the ability of zooplankton to control phytoplankton growth in colder conditions (e.g., Landry et al., 2000).

For all water masses, the loss rate decreases as the depth-integrated biomass decreases, but at a faster rate, so that the specific loss rate (L/$C_{P0/300}$, not shown) decreases with depth-integrated biomass, However,

Table 2
Summary of depth-integrated net primary production.

	STW		SAW		SAM	
	Mean ± std (mg C m^{-2} d^{-1})	Percent below 50 m	Mean ± std (mg C m^{-2} d^{-1})	Percent below 50 m	Mean ± std (mg C m^{-2} d^{-1})	Percent below 50 m
NPP_{int1}	1004 ± 609	23	265 ± 33	2	425 ± 90	2
NPP_{int2}	894 ± 304	47	296 ± 100	5	368 ± 35	9
VGPM	440 ± 156	–	316 ± 100	–	760 ± 245	–

Mean and standard deviation of depth-integrated net primary production (NPP) estimates for each model and VGPM in all water masses. Also shown is the percentage of the depth-integrated NPP found deeper than 50 m in the two models.

without direct estimates of zooplankton biomass, we cannot determine the relative roles of grazer density and biomass-specific grazing activity in these losses.

6. Conclusions

The main findings of this study are that combining BGC-Argo data with simple representations of the subsurface light field can yield reasonable first-order estimations of the vertical structure of production in the ocean, including estimates of the relative contributions of deep and near-surface production to depth-integrated NPP.

The main limitation of this work is the sparsity of *in situ* measurements of primary production to tune the models. Even so, we suggest that models with simple representations of the vertical structure in production can perform better than surface-based algorithms of NPP, and can provide useful estimates of the role of sub-surface production in depth-integrated NPP.

In summary, in the south-west Pacific Ocean, the main surface water masses bloom at opposite times of the year. In STW, an autumn bloom is initiated when the mixed layer deepens to entrain additional nutrients into the euphotic zone. For about half the year during spring and summer, there is a deep chlorophyll/biomass maximum. Consequently, depth-integrated phytoplankton biomass and depth-integrated NPP are largely decoupled from surface biomass. Model estimates of mean depth-integrated NPP range from 900 to 1000 mg C m^{-2} d^{-1}, with between 23 and 47% of the production deeper than 50 m (Table 2). VGPM estimates of depth-integrated NPP are about half the model estimates.

In contrast, in SAW and SAMW, a spring bloom is initiated when convective overturn slows (but before it ceases altogether). Model estimates of depth-integrated NPP range from 265 to 425 mg C m^{-2} d^{-1}, depending on water mass. Production is almost entirely within the mixed layer, and depth-integrated phytoplankton biomass and depth-integrated NPP follow surface biomass. VGPM estimates of depth-integrated NPP are comparable with the model estimates, except where temperature was anomalously high.

Key points

- Net primary production (NPP) estimated from BGC-Argo floats using simple conceptual models is compared to NPP estimated from satellite data
- In Subtropical Water, an autumn bloom is initiated by deepening mixing, and subsurface production accounts for over half the total production in summer
- In Subantarctic Water, a spring bloom is initiated when deep mixing ceases, and there is relatively little subsurface production through the year

Declaration of competing interest

The authors declare that they have no known competing financial interests or personal relationships that could have appeared to influence the work reported in this paper.

Acknowledgements

We thank all those who provided the ^{14}C-uptake measurements for this work, including the crews of the respective research vessels for their contributions. The ^{14}C-uptake measurements of NPP and supporting oceanographic data are available in PANGAEA (www.pangaea.de), following the FAIR principles of data archiving, under doi: 10.1594/PANGAEA.931742. The NCEP reanalysis derived heat fluxes were provided by NOAA/OAR/ESRL PSL, Boulder, Colorado, (https://psl.noaa.gov/data/gridded/data.ncep.reanalysis.surfaceflux.html).

MODIS ocean colour data (sea surface chlorophyll and PAR) were made available by NASA's Ocean Biology Processing Group (OBPG) (https://oceandata.sci.gsfc.nasa.gov/MODIS-Aqua/Mapped/8-Day/9km/). The VGPM data were made available by the Ocean Color group at Oregon State University (http://orca.science.oregonstate.edu/1080.by.2160.8day.hdf.vgpm.m.chl.m.sst.php).

The BGC-Argo data were made available by the Southern Ocean Carbon and Climate Observations and Modeling (SOCCOM) program, funded by the National Science Foundation, Division of Polar Programs (NSF PLR -1425989), supplemented by NASA, and by the International Argo Program and the NOAA programs that contribute to it. (http://www.argo.ucsd.edu, http://argo.jcommops.org).

High-resolution Matlab files (doi.org/10.6075/J0KK996D) were downloaded from SOCCOM website https://soccom.princeton.edu/content/data-access. This work was supported by the New Zealand Ministry of Business, Innovation and Employment through grant MBIE C01X1703. We thank the reviewers for their conscientious and detailed reviews.

Appendix A. Supplementary data

Supplementary data to this article can be found online at https://doi.org/10.1016/j.dsr.2022.103834.

References

Aumont, O., Ethé, C., Tagliabue, A., Bopp, L., Gehlen, M., 2015. PISCES-v2: an ocean biogeochemical model for carbon and ecosystem studies. Geosci. Model Dev. (GMD) 8 (8), 2465–2513. https://doi.org/10.5194/gmd-8-2465-2015.

Banse, K., 1982. Cell volumes, maximal growth rates of unicellular algae and ciliates, and the role of ciliates in the marine pelagial1,2. Limnol. Oceanogr. 27 (6), 1059–1071. https://doi.org/10.4319/lo.1982.27.6.1059.

Banse, K., English, D.C., 1997. Near-surface phytoplankton pigment from the coastal zone color scanner in the subantarctic region southeast of New Zealand. Mar. Ecol. Prog. Ser. 156, 51–66. https://doi.org/10.3354/meps156051.

Barton, S., Yvon-Durocher, G., 2019. Quantifying the temperature dependence of growth rate in marine phytoplankton within and across species. Limnol. Oceanogr. 64 (5), 2081–2091. https://doi.org/10.1002/lno.11170.

Behrenfeld, M., Falkowski, P.G., 1997a. A consumer's guide to phytoplankton primary productivity models. Limnol. Oceanogr. 42 (7), 1479–1491. https://doi.org/10.4319/lo.1997.42.7.1479.

Behrenfeld, M.J., Boss, E., Siegel, D.A., Shea, D.M., 2005. Carbon-based ocean productivity and phytoplankton physiology from space. Global Biogeochem. Cycles 19 (1), GB1006. https://doi.org/10.1029/2004GB002299.

Behrenfeld, M.J., Falkowski, P.G., 1997b. Photosynthetic rates derived from sateillite-based chlorophyll concentration. Limnol. Oceanogr. 42 (1), 1–20. https://doi.org/10.4319/lo.1997.42.1.0001.

Bopp, L., et al., 2013. Multiple stressors of ocean ecosystems in the 21st century: projections with CMIP5 models. Biogeosciences 10 (10), 6225–6245. https://doi.org/10.5194/bg-10-6225-2013.

Boss, E., Picheral, M., Leeuw, T., Chase, A., Karsenti, E., Gorsky, G., Taylor, L., Slade, W., Ras, J., Claustre, H., 2013. The characteristics of particulate absorption, scattering and attenuation coefficients in the surface ocean; Contribution of the Tara Oceans expedition. Methods Oceanogr. 7, 52–62. https://doi.org/10.1016/j.mio.2013.11.002.

Boss, E.B., Haëntjens, N., 2016. Primer regarding measurements of chlorophyll fluorescence and the backscattering coefficient with WETLabs FLBB on profiling floats. For. Rep. 11.
Bostock, H.C., Sutton, P.J., Williams, M.J.M., Opdyke, B.N., 2013. Reviewing the circulation and mixing of Antarctic Intermediate Water in the South Pacific using evidence from geochemical tracers and Argo float trajectories. Deep Sea Res. Oceanogr. Res. Pap. 73, 84–98. https://doi.org/10.1016/j.dsr.2012.11.007.
Boyd, P., LaRoche, J., Gall, M., Frew, R., McKay, R.M.L., 1999. Role of iron, light, and silicate in controlling algal biomass in subantarctic waters SE of New Zealand. J. Geophys. Res.: Oceans 104 (C6), 13395–13408. https://doi.org/10.1029/1999JC900009.
Boyd, P.W., McTainsh, G., Sherlock, V., Richardson, K., Nichol, S., Ellwood, M., Frew, R., 2004. Episodic enhancement of phytoplankton stocks in New Zealand subantarctic waters: contribution of atmospheric and oceanic iron supply. Global Biogeochem. Cycles 18 (1). https://doi.org/10.1029/2002GB002020.
Bradford-Grieve, J.M., Boyd, P.W., Chang, F.H., Chiswell, S.M., Hadfield, M., Hall, J.A., James, M.R., Nodder, S.D., Shuskina, E.A., 1999. Pelagic ecosystem structure and functioning in the Subtropical Front region east of New Zealand in austral winter and spring 1993. J. Plankton Res. 21 (3), 405–428. https://doi.org/10.1093/plankt/21.3.405.
Bushinsky, S.M., Emerson, S., 2015. Marine biological production from in situ oxygen measurements on a profiling float in the subarctic Pacific Ocean. Global Biogeochem. Cycles 29 (12), 2050–2060. https://doi.org/10.1002/2015GB005251.
Carberry, L., Roesler, C., Drapeau, S., 2019. Correcting in situ chlorophyll fluorescence time-series observations for nonphotochemical quenching and tidal variability reveals nonconservative phytoplankton variability in coastal waters. Limnol Oceanogr. Methods 17 (8), 462–473. https://doi.org/10.1002/lom3.10325.
Carr, M.-E., et al., 2006. A comparison of global estimates of marine primary production from ocean color. Deep Sea Res. Part II Top. Stud. Oceanogr. 53 (5), 741–770. https://doi.org/10.1016/j.dsr2.2006.01.028.
Carranza, M.M., Gille, S.T., Franks, P.J.S., Johnson, K.S., Pinkel, R., Girton, J.B., 2018. When mixed layers are not mixed. Storm-driven mixing and bio-optical vertical gradients in mixed layers of the Southern Ocean. J. Geophys. Res.: Oceans 123 (10), 7264–7289. https://doi.org/10.1029/2018jc014416.
Chassot, E., Bonhommeau, S., Dulvy, N.K., Melin, F., Watson, R., Gascuel, D., Le Pape, O., 2010. Global marine primary production constrains fisheries catches. Ecol. Lett. 13 (4), 495–505. https://doi.org/10.1111/j.1461-0248.2010.01443.x.
Chiswell, S.M., 2011. Annual cycles and spring blooms in phytoplankton: don't abandon Sverdrup completely. Mar. Ecol. Prog. Ser. 443, 39–50. https://doi.org/10.3354/meps09453.
Chiswell, S.M., Bradford-Grieve, J., Hadfield, M.G., Kennan, S.C., 2013. Climatology of surface chlorophyll a, autumn-winter and spring blooms in the southwest Pacific Ocean. J. Geophys. Res.: Oceans 118 (2), 1003–1018. https://doi.org/10.1002/jgrc.20088.
Chiswell, S.M., Calil, P.H.R., Boyd, P.W., 2015. Spring blooms and annual cycles of phytoplankton: a unified perspective. J. Plankton Res. 37 (3), 500–508. https://doi.org/10.1093/plankt/fbv021.
Claustre, H., Johnson, K.S., Takeshita, Y., 2020. Observing the global ocean with biogeochemical-argo. Ann. Rev. Mar. Sci 12 (1), 23–48. https://doi.org/10.1146/annurev-marine-010419-010956.
Dugdale, R.C., Wilkerson, F.P., Minas, H.J., 1995. The role of a silicate pump in driving new production. Deep Sea Res. Oceanogr. Res. Pap. 42 (5), 697–719. https://doi.org/10.1016/0967-0637(95)00015-X.
Ellwood, M.J., et al., 2018. Insights into the biogeochemical cycling of iron, nitrate, and phosphate across a 5,300 km south pacific zonal section (153°E-150°W). Global Biogeochem. Cycles 32 (2), 187–207. https://doi.org/10.1002/2017gb005736.
Ellwood, M.J., Boyd, P.W., Sutton, P., 2008. Winter-time dissolved iron and nutrient distributions in the Subantarctic Zone from 40–52S; 155–160E. Geophys. Res. Lett. 35 (11) https://doi.org/10.1029/2008gl033699.
Ellwood, M.J., Hutchins, D.A., Lohan, M.C., Milne, A., Nasemann, P., Nodder, S.D., Sander, S.G., Strzepek, R., Wilhelm, S.W., Boyd, P.W., 2015. Iron stable isotopes track pelagic iron cycling during a subtropical phytoplankton bloom. Proc. Natl. Acad. Sci. U.S.A. 112 (1), E15–E20. https://doi.org/10.1073/pnas.1421576112.
Ellwood, M.J., Law, C.S., Hall, J., Woodward, E.M.S., Strzepek, R., Kuparinen, J., Thompson, K., Pickmere, S., Sutton, P., Boyd, P.W., 2013. Relationships between nutrient stocks and inventories and phytoplankton physiological status along an oligotrophic meridional transect in the Tasman Sea. Deep Sea Res. Oceanogr. Res. Pap. 72, 102–120. https://doi.org/10.1016/j.dsr.2012.11.001.
Goldman, J.C., McCarthy, J.J., Peavey, D.G., 1979. Growth rate influence on the chemical composition of phytoplankton in oceanic waters. Nature 279 (5710), 210–215. https://doi.org/10.1038/279210a0.
Graff, J.R., Westberry, T.K., Milligan, A.J., Brown, M.B., Dall'Olmo, G., Dongen-Vogels, V.v., Reifel, K.M., Behrenfeld, M.J., 2015. Analytical phytoplankton carbon measurements spanning diverse ecosystems. Deep Sea Res. Oceanogr. Res. Pap. 102, 16–25. https://doi.org/10.1016/j.dsr.2015.04.006.
Gutiérrez-Rodríguez, A., Safi, K., Fernández, D., Forcén-Vázquez, A., Gourvil, P., Hoffmann, L., Pinkerton, M., Sutton, P., Nodder, S.D., 2020. Decoupling between phytoplankton growth and microzooplankton grazing Enhances productivity in subantarctic waters on Campbell Plateau, southeast of New Zealand. J. Geophys. Res.: Oceans 125 (2), e2019JC015550. https://doi.org/10.1029/2019jc015550.
Heath, R.A., 1985. A review of the physical oceanography of the seas around New Zealand — 1982. N. Z. J. Mar. Freshw. Res. 19 (1), 79–124. https://doi.org/10.1080/00288330.1985.9516077.
Heath, R.A., Bradford, J.M., 1980. Factors influencing phytoplankton production over the Campbell Plateau, New Zealand. J. Plankton Res. 2 (2), 169–181. https://doi.org/10.1093/plankt/2.2.169.
Johnson, K.S., et al., 2017a. Biogeochemical sensor performance in the SOCCOM profiling float array. J. Geophys. Res.: Oceans 122 (8), 6416–6436. https://doi.org/10.1002/2017JC012838.
Johnson, K.S., Plant, J.N., Dunne, J.P., Talley, L.D., Sarmiento, J.L., 2017b. Annual nitrate drawdown observed by SOCCOM profiling floats and the relationship to annual net community production. J. Geophys. Res.: Oceans 122 (8), 6668–6683. https://doi.org/10.1002/2017JC012839.
Kahru, M., Kudela, R., Manzano-Sarabia, M., Mitchell, B.G., 2009. Trends in primary production in the California Current detected with satellite data. J. Geophys. Res. 114 (C2), 1–7. https://doi.org/10.1029/2008JC004979.
Kalnay, E., et al., 1996. The NCEP/NCAR 40-year reanalysis project. Bull. Am. Meteorol. Soc. 77 (3), 437–471. https://doi.org/10.1175/1520-0477(1996)077<0437:tnyrp>2.0.co;2.
Kara, A.B., Rochford, P.A., Hurlburt, H.E., 2000. An optimal definition for ocean mixed layer depth. J. Geophys. Res.: Oceans 105 (C7), 16803–16821. https://doi.org/10.1029/2000JC900072.
Krumhardt, K.M., Lovenduski, N.S., Long, M.C., Lindsay, K., 2017. Avoidable impacts of ocean warming on marine primary production: insights from the CESM ensembles. Global Biogeochem. Cycles 31 (1), 114–133. https://doi.org/10.1002/2016gb005528.
Landry, Ondrusek, M., Tanner, S.J., Brown, S., Constantinou, J., Bidigare, R., Coale, K., Fitzwater, S., 2000. Biological response to iron fertilization in the eastern equatorial Pacific (IronEx II). I. Microplankton community abundances and biomass. Mar. Ecol. Prog. Ser. 201, 27–42. https://doi.org/10.3354/meps201027.
Law, C.S., Rickard, G.J., Mikaloff-Fletcher, S.E., Pinkerton, M.H., Behrens, E., Chiswell, S. M., Currie, K., 2017. Climate change projections for the surface ocean around New Zealand. N. Z. J. Mar. Freshw. Res. 1–27. https://doi.org/10.1080/00288330.2017.1390772.
Laws, E.A., 2013. Evaluation of in situ phytoplankton growth rates: a synthesis of data from varied approaches. Ann. Rev. Mar. Sci 5, 247–268. https://doi.org/10.1146/annurev-marine-121211-172258.
Li, Q.P., Franks, P.J.S., Landry, M.R., Goericke, R., Taylor, A.G., 2010. Modeling phytoplankton growth rates and chlorophyll to carbon ratios in California coastal and pelagic ecosystems. J. Geophys. Res. 115 (G4) https://doi.org/10.1029/2009jg001111.
Litchman, E., Klausmeier, C.A., 2008. Trait-based community Ecology of phytoplankton. Annu. Rev. Ecol. Evol. Syst. 39 (1), 615–639. https://doi.org/10.1146/annurev.ecolsys.39.110707.173549.
Longhurst, A.R., 2007. Ecological Geography of the Sea. Academic Press, p. 542. https://doi.org/10.1016/B978-0-12-455521-1.X5000-1.
Milutinović, S., Behrenfeld, M.J., Johannessen, J.A., Johannessen, T., 2009. Sensitivity of remote sensing–derived phytoplankton productivity to mixed layer depth: lessons from the carbon-based productivity model. Global Biogeochem. Cycles 23 (4). https://doi.org/10.1029/2008gb003431.
Morel, A., Maritorena, S., 2001. Bio-optical properties of oceanic waters: a reappraisal. J. Geophys. Res.: Oceans 106 (C4), 7163–7180. https://doi.org/10.1029/2000jc000319.
Morris, M., Stanton, B., Neil, H., 2001. Subantarctic oceanography around New Zealand: preliminary results from an ongoing survey. N. Z. J. Mar. Freshw. Res. 35 (3), 499–519. https://doi.org/10.1080/00288330.2001.9517018.
Murphy, R.J., Pinkerton, M.H., Richardson, K.M., Bradford-Grieve, J.M., Boyd, P.W., 2001. Phytoplankton distributions around New Zealand derived from SeaWiFS remotely-sensed ocean colour data. N. Z. J. Mar. Freshw. Res. 35 (2), 343–362. https://doi.org/10.1080/00288330.2001.9517005.
Nodder, S.D., Boyd, P.W., Chiswell, S.M., Pinkerton, M.H., Bradford-Grieve, J.M., Greig, M.J.N., 2005. Temporal coupling between surface and deep ocean biogeochemical processes in contrasting subtropical and subantarctic water masses, southwest Pacific Ocean. J. Geophys. Res. 110 (C12), C12017 https://doi.org/10.1029/2004jc002833, 12015.
Nodder, S.D., Chiswell, S.M., Northcote, L.C., 2016. Annual cycles of deep-ocean biogeochemical export fluxes in subtropical and subantarctic waters, southwest Pacific Ocean. J. Geophys. Res.: Oceans 121 (4), 2405–2424. https://doi.org/10.1002/2015jc011243.
Peloquin, J., Hall, J., Safi, K., Smith, W.O., Wright, S., van den Enden, R., 2011. The response of phytoplankton to iron enrichment in Sub-Antarctic HNLCLSi waters: results from the SAGE experiment. Deep Sea Res. Part II Top. Stud. Oceanogr. 58 (6), 808–823. https://doi.org/10.1016/j.dsr2.2010.10.021.
Phung, A., 2020. A comparison of biogeochemical Argo sensors, remote sensing systems, and shipborne field fluorometers to measure chlorophyll a concentrations in the Pacific Ocean off the northern coast of New Zealand. In: Paper Presented at Global Oceans 2020: Singapore – U.S. Gulf Coast, 5-30 Oct. 2020.
Priede, I.G., et al., 2013. Does presence of a mid-ocean ridge enhance biomass and biodiversity? PLoS One 8 (5). https://doi.org/10.1371/journal.pone.0061550 e61550-e61550.
Rintoul, S.R., Trull, T.W., 2001. Seasonal evolution of the mixed layer in the Subantarctic zone south of Australia. J. Geophys. Res.: Oceans 106 (C12), 31447–31462. https://doi.org/10.1029/2000jc000329.
Roesler, C., et al., 2017. Recommendations for obtaining unbiased chlorophyll estimates from in situ chlorophyll fluorometers: a global analysis of WET Labs ECO sensors. Limnol Oceanogr. Methods 15 (6), 572–585. https://doi.org/10.1002/lom3.10185.
Rose, J.M., Caron, D.A., 2007. Does low temperature constrain the growth rates of heterotrophic protists? Evidence and implications for algal blooms in cold waters. Limnol. Oceanogr. 52 (2), 886–895. https://doi.org/10.4319/lo.2007.52.2.0886.
Salinger, M.J., et al., 2019. The unprecedented coupled ocean-atmosphere summer heatwave in the New Zealand region 2017/18: drivers, mechanisms and impacts. Environ. Res. Lett. 14 (4) https://doi.org/10.1088/1748-9326/ab012a.

Sathyendranath, S., Stuart, V., Nair, A., Oka, K., Nakane, T., Bouman, H., Forget, M.H., Maass, H., Platt, T., 2009. Carbon-to-chlorophyll ratio and growth rate of phytoplankton in the sea. Mar. Ecol. Prog. Ser. 383, 73–84. https://doi.org/10.3354/Meps07998.

Stevens, C.L., Sutton, P.J.H., Law, C.S., 2012. Internal waves downstream of Norfolk Ridge, western Pacific, and their biophysical implications. Limnol. Oceanogr. 57 (4), 897–911. https://doi.org/10.4319/lo.2012.57.4.0897.

Stock, C.A., John, J.G., Rykaczewski, R.R., Asch, R.G., Cheung, W.W., Dunne, J.P., Friedland, K.D., Lam, V.W., Sarmiento, J.L., Watson, R.A., 2017. Reconciling fisheries catch and ocean productivity. Proc. Natl. Acad. Sci. U.S.A. 114 (8), E1441–E1449. https://doi.org/10.1073/pnas.1610238114.

Suga, T., Motoki, K., Aoki, Y., Macdonald, A.M., 2004. the north pacific climatology of winter mixed layer and mode waters. J. Phys. Oceanogr. 34 (1), 3–22. https://doi.org/10.1175/1520-0485(2004)034<0003:TNPCOW>2.0.CO;2.

Taboada, F.G., Barton, A.D., Stock, C.A., Dunne, J., John, J.G., 2019. Seasonal to interannual predictability of oceanic net primary production inferred from satellite observations. Prog. Oceanogr. 170, 28–39. https://doi.org/10.1016/j.pocean.2018.10.010.

Thomalla, S.J., Moutier, W., Ryan-Keogh, T.J., Gregor, L., Schütt, J., 2018. An optimized method for correcting fluorescence quenching using optical backscattering on autonomous platforms. Limnol Oceanogr. Methods 16 (2), 132–144. https://doi.org/10.1002/lom3.10234.

Tseng, H., You, W., Chang, C., Chuang, K., Yeh, H., Gong, G., 2019. Applicability Assessment for Global Standard Algorithm of Marine Primary Production in the Seas Surrounding Taiwan Around the Tropic of Cancer in the Northwest Pacific, Paper Presented at OCEANS 2019 - Marseille, 17-20 June 2019.

Weiskerger, C.J., Rowe, M.D., Stow, C.A., Stuart, D., Johengen, T., 2018. Application of the beer–lambert model to attenuation of photosynthetically active radiation in a shallow, Eutrophic lake. Water Resour. Res. 54 (11), 8952–8962. https://doi.org/10.1029/2018WR023024.

Wolf, K.U., Woods, J.D., 1988. Lagrangian simulation of primary production in the physical environment — the deep chlorophyll maximum and nutricline. In: Rothschild, B.J. (Ed.), Toward a Theory on Biological-Physical Interactions in the World Ocean. Springer Netherlands, pp. 51–70. https://doi.org/10.1007/978-94-009-3023-0_4.

Xing, X., Morel, A., Claustre, H., Antoine, D., D'Ortenzio, F., Poteau, A., Mignot, A., 2011. Combined processing and mutual interpretation of radiometry and fluorimetry from autonomous profiling Bio-Argo floats: Chlorophyllaretrieval. J. Geophys. Res. 116 (C6) https://doi.org/10.1029/2010jc006899.

Xing, X.G., Claustre, H., Blain, S., D'Ortenzio, F., Antoine, D., Ras, J., Guinet, C., 2012. Quenching correction for in vivo chlorophyll fluorescence acquired by autonomous platforms: a case study with instrumented elephant seals in the Kerguelen region (Southern Ocean). Limnol Oceanogr. Methods 10, 483–495. https://doi.org/10.4319/lom.2012.10.483.

Yang, B., Boss, E.S., Haëntjens, N., Long, M.C., Behrenfeld, M.J., Eveleth, R., Doney, S.C., 2020. Phytoplankton phenology in the north atlantic: insights from profiling float measurements. Front. Mar. Sci. 7 https://doi.org/10.3389/fmars.2020.00139.